Atmospheric Research 316 (2025) 107936

Contents lists available at ScienceDirect

Atmospheric Research

journal homepage: www.elsevier.com/locate/atmosres

Convection-permitting climate simulations over South America: Experimentation during different phases of ENSO☆

Changhai Liu [a,*], Kyoko Ikeda [a], Andreas Prein [a], Lucia Scaff [b], Francina Dominguez [c], Roy Rasmussen [a], Yongjie Huang [d], Jimy Dudhia [a], Wei Wang [a], Fei Chen [e], Lulin Xue [a], Lluís Fita [f], Miguel Lagos-Zúñiga [g], Waldo Lavado-Casimiro [h], Mariano Masiokas [i], Franciano Puhales [j], Leidy Johanna Yepes [k]

[a] NSF National Center for Atmospheric Research, Boulder, CO, United States
[b] University of Concepción, Concepción, Chile
[c] University of Illinois at Urban Champaign, Urbana, United States
[d] University of Oklahoma, Norman, United States
[e] Division of Environment and Sustainability, The Hong Kong University of Science and Technology, Hong Kong
[f] Universidad de Buenos Aires, Centro de Investigaciones del Mar y la Montaña, IFAECI, UBA-CONICET-CNRS-IRD, Buenos Aires, Argentina
[g] Universidad Técnica Federico Santa María, Departamento de Obras Civiles, San Joaquín, Chile
[h] Servicio Nacional de Meteorología e Hidrología del Perú, Lima, Peru
[i] Instituto Argentino de Nivología, Glaciología y Ciencias Ambientales, Mendoza, Argentina
[j] Universidade Federal de Santa Maria, Santa Maria, Brazil
[k] National University of Colombia, Bogota, Colombia

ARTICLE INFO

Keywords:
South America
Convection permitting
WRF model
Regional climate simulation

ABSTRACT

This paper presents the first-ever continental-scale convection-permitting simulations over South America for three water years of different ENSO phases, corresponding to an ENSO neutral year (2018/19), an EI Niño year (2015/16), and a La Niña year (2010/11), using the Weather Research and Forecasting (WRF) model at 4-km grid spacing. The model performance has been validated against precipitation derived from satellite, surface observations, and surface air temperature from reanalysis. The evaluation shows a promising skill at reproducing the observed multi-scale spatiotemporal characteristics of precipitation and temperature, such as the seasonal and sub-seasonal variability, the diverse patterns of diurnal cycle, and deep convective clouds. Sensitivity simulations quantify the impacts of cumulus parameterization, grid spacing, and spectral nudging. Results indicate that a tested scale-aware convection scheme has little benefit, and the model performance degrades as horizontal resolution decreases. Spectral nudging can reduce the precipitation bias over some tropical and subtropical regions but exacerbates the wet bias over the Andean Mountains. A noteworthy model deficiency shared in all simulations is the excess orographic precipitation, a problem in association with the overly active afternoon-evening convection possibly resultant from under-representation of clouds and missing cloud-aerosol interaction, though the uncertainty of observational data might contribute to the wet bias as well. These results provide useful guidance for improving the model physics. The overall encouraging agreement between the 4-km model simulations and observations provides confidence in the usage of the established model configuration for regional climate downscaling and climate change projections over South America.

1. Introduction

South America is the world's fourth largest continent, extending from the northern equatorial area, across the equator, and into the sub-Arctic. Bordered by the Atlantic Ocean to the east, the Pacific Ocean to the west, and the Antarctic Ocean to the south, the continent contains the world's longest mountain range, the Andes, on the western edge, the extensive highlands in the east, and a central lowland in-between(10°N-

☆ The National Center for Atmospheric Research is sponsored by the National Science Foundation.

* Corresponding author at: NSF National Center for Atmospheric Research, P. O. Box 3000, Boulder, CO 80307-3000, United States.
E-mail address: chliu@ucar.edu (C. Liu).

https://doi.org/10.1016/j.atmosres.2025.107936
Received 23 September 2024; Received in revised form 31 December 2024; Accepted 18 January 2025
Available online 23 January 2025

25°S), where strong convection activity provides rainfall for the Amazon. These unique geographical attributes and the large landmass size mostly dictate the diverse characteristics of the South American climate system, ranging from the dominant rainy and humid conditions in the tropics, the cold-dry snow-covered mountains in the Andes and the world's driest desert conditions over the Atacama Desert (Garreaud et al., 2009; Espinoza et al., 2020; Arias et al., 2021).

Owing to its multiple ecosystems, South America plays an important role in the global climate and water cycle. In particular, it is home to the largest and most biodiverse tropical rainforest on the planet, the Amazon rainforest, where about 15 % of global terrestrial photosynthesis takes place, playing a crucial role in modulating the global carbon cycle and carbon-climate feedback (Field et al., 1998). The vast amount of carbon stored in the tropical forest is recognized as a potential tipping point in the global climate system (Malhi et al., 2006; Lenton et al., 2008; Boulton et al., 2013). The massive water and energy exchange between tropical forests and the atmosphere through the precipitation that falls in the forest and evapotranspiration re-distributes the water throughout the continent, accounting for approximately 30 % of the precipitation within the Amazon basin and about 16 % of the precipitation in La Plata basin (Yang and Dominguez, 2019). The freshwater discharge from the Amazon, Orinoco, and Parana rivers accounts for about 22 % of global continental discharge into the oceans (Dai and Trenberth, 2002), being an essential component of the global terrestrial water cycle. The Andes accommodates most tropical glaciers and snow-fed watersheds, with the seasonal melting providing a significant supply of freshwater during the dry season for a large population living around the Andes (Dussaillant et al., 2019; Masiokas et al., 2020; Espinoza et al., 2020). At higher latitudes, in the western Andes of Chile, the synoptic activity modulates the precipitation's occurrence, characterizing a strong seasonal behavior with large precipitation amounts in the Austral winter in mid-latitudes, while southern South America is dominated by the south hemisphere storm track (Garreaud et al., 2009).

The South American climate system encompasses complex interactions between various atmospheric and land-surface processes, topographic forcing, precipitating convection including organized mesoscale convective systems (MCSs), diurnal cycle of convection, and aerosols. The proper representation of the above multi-scale processes and their interactions presents a great challenge for global climate models (GCMs) largely due to the coarse resolution and dependency on conventional convective parameterization. State-of-the-art GCMs generally have a grid spacing of 50–200 km, which limits their ability to capture many important mesoscale features that are crucial for local and regional climate systems, resulting in various deficiencies. For instance, the Coupled Model Intercomparison Project Phase 3 (CMIP3) models were shown to have highly variable biases (Vera et al., 2006), unable to reproduce quantitatively accurate seasonal precipitation over the main basins of the continent (i.e., the Amazon and La Plata basins), CMIP5 models commonly underestimate total rainfall during the dry and transition seasons (Yin et al., 2013), and CMIP6 models have shown a wet bias in arid regions and underestimation of precipitation in mid-latitudes in the western Andes, with low performance in reproducing large scale teleconnections (Gateño et al., 2024).

Dynamical downscaling using regional climate models (RCMs), first pioneered by Dickinson et al. (1989) and Giorgi and Bates (1989), has been pursued to overcome the GCM's deficiencies and improve the regional climate simulations via the usage of higher spatial resolution and improved treatment of sub-grid scale physics. This approach has experienced rapid thriving and extensive applications and steadily evolving toward an increase of simulation length and an expansion of computational domain along with a refinement of spatial resolution during the past few decades (Xue et al., 2014; Giorgi, 2019). Particularly, with a steady advancement of computer resources since the 2010s, regional climate modeling has started to operate in a grid-spacing range of ~4 km or below with explicit representation of convection (Prein and Coauthors, 2015; Schär and Co-authors, 2020). Such high-resolution RCMs are often termed convection-permitting models (CPMs) that have long been used for operational numerical weather prediction and short-term weather forecasting type of simulations (e.g., Done et al., 2004; Liu et al., 2006; Kain and Coauthors, 2008). CPMs have been successfully applied to climate downscaling over different geographical regions, such as North America (e.g., Ikeda et al., 2010, 2021; Rasmussen et al., 2011, 2014; Liu et al., 2017; Wang et al., 2018), Europe (e.g., Kendon et al., 2012, 2014; Chan et al., 2014; Coppola and Coauthors, 2020; Ban et al., 2014, 2021), East Asia (e.g., Yun et al., 2020; Guo et al., 2020), and Africa (e.g., Stratton et al., 2018). Significant improvements relative to traditional coarse-resolution downscaling with parameterized convection were clearly demonstrated in these previous studies at simulating orographically enhanced precipitation and snowpack, diurnal cycle of precipitation, precipitation frequency and intensity, and extreme precipitation on daily and sub-daily timescales, as well as MCSs (e.g., Prein et al., 2017; Yun et al., 2021), all of which are primarily attributed to the better representation of various small-scale and mesoscale processes and avoidance of convective parameterization.

In contrast to its wide applications in other parts of the world, however, convection-permitting downscaling over South America is rather limited. Up to now, RCM exercises over this continent, such as those in the CORDEX (Coordinated Regional Climate Downscaling Experiment), are mostly performed with 20–50 km or even coarser grid spacings (Solman, 2013; Ambrizzi et al., 2018), which are unsuitable for properly depicting complex land-water distributions and mountain-valley contrasts and associated mesoscale circulations in South America, and still need error-prone convective parameterization for dealing with subgrid-scale convective processes. As a result, these regional climate simulations suffer various uncertainties similar to global models; for example, Solman (2013) showed that the ensemble mean of seven RCM simulations with 50-km grid spacing systematically underestimates the seasonal precipitation over most of the continent but overestimates the orographic precipitation over the Andes. All existing convection-permitting modeling attempts, albeit very few, were restricted to small sub-continental domains and short simulation period (e.g., Portele et al., 2021; Feijoó and Solman, 2022; Huang et al., 2023, 2024a, 2024b). One exception is the recent work by Halladay et al. (2023), where convection-permitting climate simulations with the Met Office United Model were performed at a near-continental scale of South America, demonstrating advantages in the representation of precipitation as compared to coarser resolution regional and global climate models.

In short, because of the very limited efforts thus far, the full benefits and potential limitations of CPM in the South American continent have not been thoroughly explored. This has motivated us to conduct multiple year-long experiments of continental-scale convection-permitting downscaling in this area. The primary objectives are: 1) to investigate the capability of convection-permitting Weather Research and Forecasting (WRF) model in reproducing the spatiotemporal characteristics of surface precipitation and temperature, with a focus on a newly established model configuration specifically for South America; 2) to examine the potential benefit of scale-sensitive cumulus parameterization and spectral nudging; 3) to assess the added value of convection-permitting resolution relative to coarser resolution; and 4) to provide guidance for improving the subgrid physics and model setup to improve the model performance. In view of the notable modulation of the El Niño–Southern Oscillation (ENSO) to the South American climate (Cai et al., 2020), multiple individual years representative of different ENSO phases were selected for experimentation to ensure achievement of general conclusions about the model performance.

The remainder of the paper is structured as follows. Section 2 presents the numerical approach and the observational data for model validation. Section 3 evaluates the simulated spatiotemporal characteristics of precipitation, surface air temperature, and deep convective clouds. The sensitivity experiments are provided in Section 4. Lastly, a summary and discussion of potential model improvements are given in

Section 5.

2. Numerical experiments and verification data

2.1. Numerical model setup

This study used the WRF model version 4.1.5 (Skamarock et al., 2019), which was configured with a single domain of 1472 × 2028 grid points at 4-km grid spacing, covering the entire South American continent and adjacent waters as shown in Fig. 1. There are 61 vertical levels capped at 10 hPa, stretching from about 50-m spacing near the surface to roughly 700-m spacing at the model top. The selection of physics parameterizations was built upon our experience from convection-permitting simulations over North America (Liu et al., 2017; Rasmussen et al., 2023) and a series of testing simulations for a rainy period of November–December 2018 using the same domain setup as in Fig. 1, consisting of the Thompson microphysics (Thompson et al., 2008), the Yonsei University (YSU) planetary boundary layer scheme (Hong et al., 2006), the Noah-MP land surface model (Niu et al., 2011), the Rapid Radiative Transfer Model for GCMs (RRTMG) longwave and shortwave atmospheric radiation (Iacono et al., 2008), and the MMF groundwater scheme (Miguez-Macho et al., 2007; Barlage et al., 2021) representing a shallow aquifer and its interaction with soil.

Numerical experiments were performed for three individual water years, beginning in the month of June, when the precipitation is confined to the northernmost continent and the western Andes (south of 30°S), and most of the continent undergoes a dry episode, and ending in the following May. The continental hydroclimate is strongly modulated by ENSO activity (e.g., Grimm and Zilli, 2009; Cai et al., 2020). For example, during the canonical El Niño (La Niña), precipitation tends to increase (decrease) in the La Plata Basin and decrease (increase) over northern South America across all seasons (Tedeschi et al., 2013). Accordingly, we chose the three years of different ENSO phase, corresponding to an ENSO neutral year (2018/19), a strong positive ENSO phase (EI Niño; 2015/16), and a strong negative ENSO phase (La Niña; 2010/11), for experimentation. These simulations, called EXP1–3 hereafter respectively (see Table 1), enable us to assess the possible dependency of model settings on the ENSO phase and make general and robust conclusions of the model performance as compared to performing simulations for an individual year only.

As shown in Table 1, four additional experiments (EXP4–7) were conducted for the 2018–2019 water year, including a simulation with spectral nudging being activated, a simulation with a scale-dependent convection scheme being applied, and two coarser resolution simulations using either 12 or 24-km grid spacing, as well as a simulation (EXP8) of the 2010–2011 water year with a high cloud droplet concentration in the microphysics parameterization. These sensitivity simulations were designed to quantify the possible benefit of spectral nudging, the value of scale-aware cumulus parameterization, the impact of horizontal resolution, and the indirect impact of aerosol. The

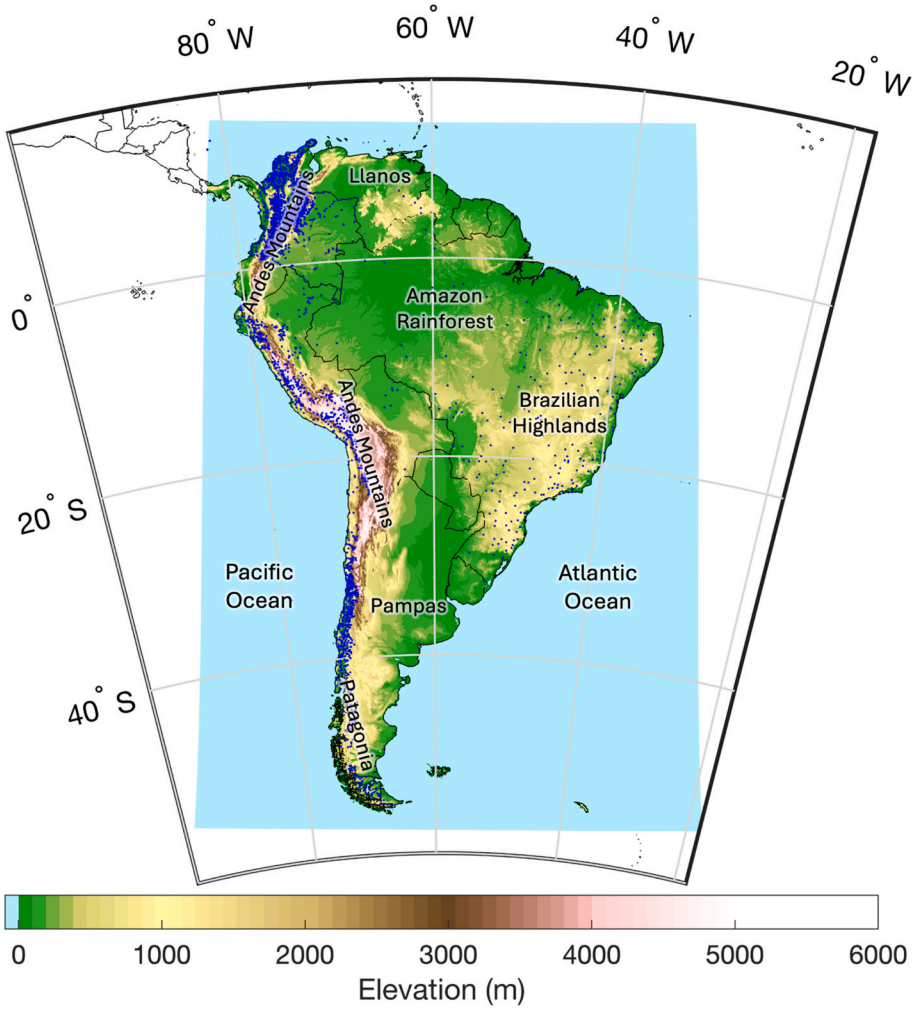

Fig. 1. Model domain (blue rectangular area) used in the simulations at 4-km grid spacing. The colour shading shows the elevation above mean sea level in meters. The dot points represent locations of the surface stations where the observational precipitation data are collected for model verification. (For interpretation of the references to colour in this figure legend, the reader is referred to the web version of this article.)

Table 1
List of the numerical experiments, showing the information of simulation period, horizontal grid spacing, deep convective parameterization scheme (DCPS), spectral nudging, and microphysics.

Experiment	Water year	Grid spacing	DCPS	Spectral nudging	Microphysics modification
EXP1	June 2018 – May 2019	4 km	no	no	n/a
EXP2	June 2015 – May 2016	4 km	no	no	n/a
EXP3	June 2010 – May 2011	4 km	no	no	n/a
EXP4	June 2018 – May 2019	4 km	no	yes	n/a
EXP5	June 2018 – May 2019	4 km	scale-aware Tiedtke	no	n/a
EXP6	June 2018 – May 2019	12 km	Tiedtke	no	n/a
EXP7	June 2018 – May 2019	24 km	Tiedtke	no	n/a
EXP8	June 2010 – May 2011	4 km	no	no	increased cloud droplets

boundary and initial conditions for all simulations were derived from the hourly, 0.25-degree fifth generation of the European Centre for Medium-Range Weather Forecasts (ECMWF) atmospheric reanalysis ERA5 (Hersbach and Co-authors, 2010), which is archived at the Research Data Archive (RDA) of the Computational and Information Systems Laboratory (CISL) of the NSF National Center for Atmospheric Research (NCAR) (https://rda.ucar.edu/datasets/ds633.0/).

2.2. Verification data

Multiple data sets from in-situ observations, satellite observations, and reanalysis were collected for simulation verification. Specifically, version 06B of the Integrated Multi-satellitE Retrievals for GPM (IMERG) gridded precipitation product (Huffman et al., 2019), which has a 30-min temporal resolution on a 0.1^{o}x0.1^{o} grid over the globe, was chosen to validate the multi-scale spatiotemporal characteristics of precipitation from seasonal to sub-daily scales. Simulation data were conservatively interpolated to the IMERG grid for point-to-point spatial comparisons using the ESMF_regrid function of the NCL software package. The hourly ERA5 data were utilized to evaluate the simulated 2-m temperature. The ERA5 surface air temperature and elevation were firstly bilinearly interpolated to model grid, and topographic corrections to the interpolated temperature were then performed based on the elevation difference between the ERA5 and WRF grids and assuming a lapse rate of 6.5 °C km^{-1}. In addition, observational data of daily precipitation at the 1331 station sites for the 2018/19 water year (dots in Fig. 1) were collected for evaluating the model performance as a complement to the satellite precipitation data. Of note is that the available surface observations are mainly located in Colombia, Peru, Chile and Brazil, but are sporadic or nearly completely absent in Argentina and the central and northeastern Amazon due to either difficulty in obtaining the data from these areas or too many missing records over the time period of study. Model values at station sites were the inverse-distance weighted average of the four closest grid points from each site location.

3. Evaluation of the experimental results

In this section, we examine the skill of the 4-km WRF model at capturing the observed seasonal and sub-seasonal distributions and diurnal variations of surface precipitation and near-surface temperature during different phases of ENSO, as well as the daily and sub-daily precipitation and convective clouds. The ENSO neutral water year (2018–2019) is presented to exemplify the model performance for most of the evaluation metrics, with the corresponding results for the other two water years, 2020/11 and 2015/16, being displayed in the supplement materials. The IPCC climate reference regions (Iturbide et al., 2020), as illustrated in Fig. S1, are utilized for subregional analysis.

3.1. Spatiotemporal characteristics of precipitation

Fig. 2 compares the monthly total precipitation of the 2018–2019 water year from the WRF simulation (EXP1 in Table 1) to the IMERG observations. In association with the ITCZ activity and the progression of monsoonal flow, observed precipitation in South America features striking seasonality. In the months of June and July (the early-middle austral winter), precipitation is largely confined within a zonally oriented area north of the equator, roughly collocated with the ITCZ, with heavy precipitation being in southern Venezuela, and eastern and Pacific coastal regions of Colombia. Other parts of the continent experience a dry episode during this time of the year. From August (the late austral winter), the tropical rain band undergoes a weakening, concurrent with a southward extension toward the Amazon Basin. The meridional expansion continues with the seasonal progression and reaches about 40^{o}S in October (mid-spring), marking the onset of the rainy season in southern South America. The seasonal precipitation persists throughout the austral summer and early fall, subsequently undergoing a sudden northward retreat to the north of 10^{o}S in late fall. Overall, the observed precipitation distribution and its seasonal and sub-seasonal variations for this particular year bear a great resemblance to the counterparts of 2015–2016 and 2010–2011 water years (Figs. S2–S3). For the most part, the model realistically reproduces the observed annual precipitation cycle. Specifically, WRF successfully captures the spatial patterns of monthly precipitation as evidenced by the high pattern correlations (Table 2), particularly during June and July, and the seasonal meridional migration, such as the southward development in the spring and the equatorward withdrawal in the fall. The model is also able to replicate the all-year-round intense precipitation belt in the tropics and its seasonal movement associated with the ITCZ, and the elongated rain band across Southeast Brazil into the Atlantic associated with the South Atlantic convergence zone (SACZ) in the warm season. The model performs consistently well throughout the year, with a slightly better skill in the austral winter than in other seasons in terms of the pattern correlation, mean absolute error (MAE), and root mean square error (RMSE) as demonstrated in Table 2. One notable deficiency is the excessive precipitation over most of the Amazon and the Andes, which is particularly conspicuous in the rainy season, leading to an areal mean wet bias for most months (Table 2). However, some differences between WRF and IMERG data may not truly represent the model deficiency considering the large uncertainties in satellite-estimated precipitation (see later discussion).

The El Niño and La Niña year (Figs. S2–S3) share many common features with the ENSO neutral year in the observed spatiotemporal precipitation variations. Especially, the heavy precipitation distribution in the tropical area and the timing for subtropical precipitation onset and retreat are all comparable between the three water years. Nonetheless, there are discernible differences. For example, the El Niño year (Fig. S2) has relatively weaker precipitation in the western Amazon

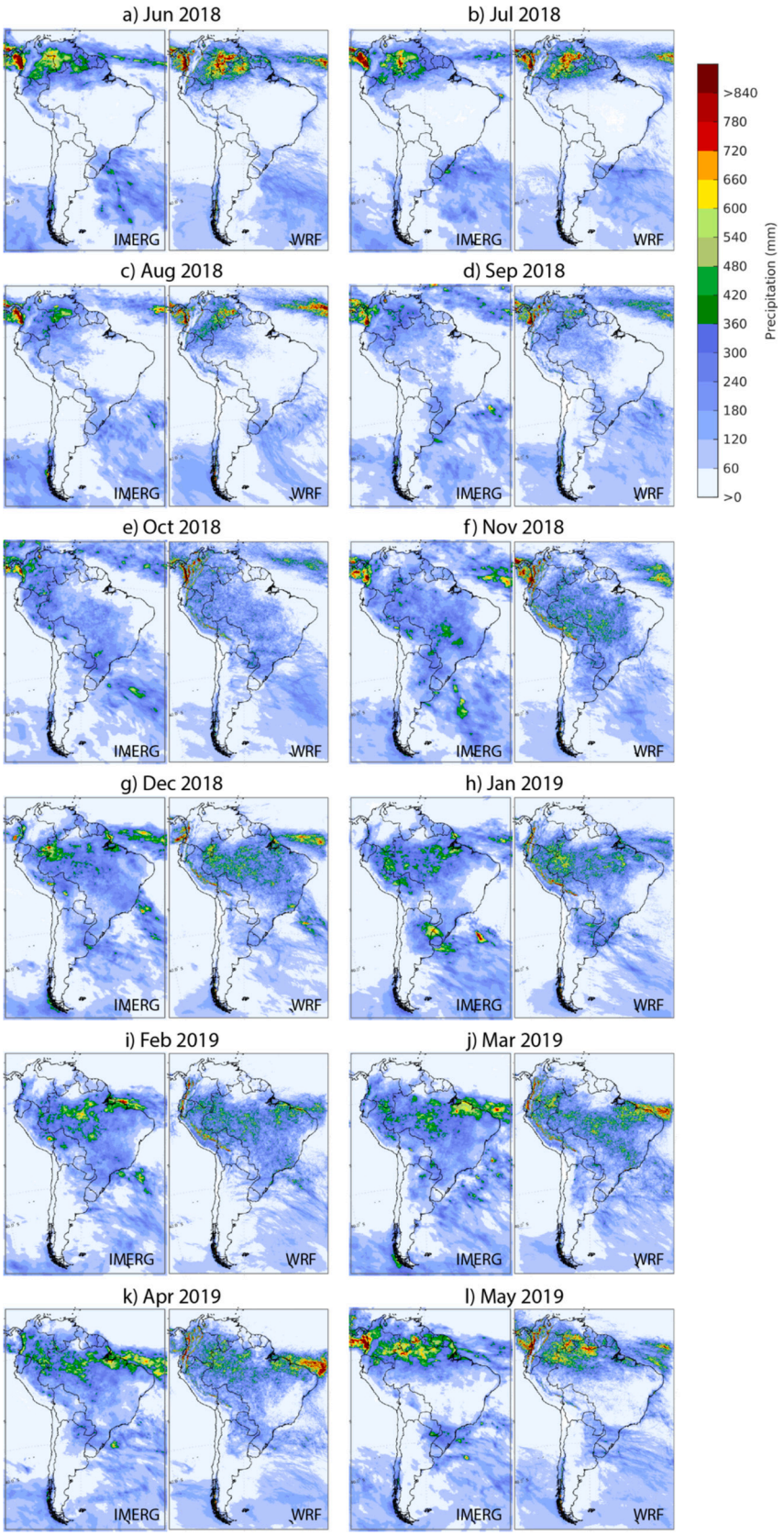

Fig. 2. Monthly total precipitation (mm) for the ENSO neutral water year (June 2018 – May 2019). Left and right panels are for IMERG and simulation (EXP1), respectively.

Table 2
Statistical results of monthly precipitation over land points of the model domain for EXP1–3, including Pearson's correlation coefficient, root mean square error (RMSE), mean bias, and mean absolute error (MAE) of the monthly total precipitation with respect to IMERG data. Black, red, and blue are for the June 2018 – May 2019, June 2015 – May 2016, and June 2010 – May 2011 water year, respectively.

Month	Corr. Coef.	RMSE (mm)	Mean Bias (mm)	MAE (mm)
June	0.866 0.837 0.847	79.7 83.5 86.1	7.7 -3.8 6.2	41.6 45.7 44.0
July	0.857 0.800 0.862	72.9 88.3 83.8	0.8 -7.1 4.8	35.8 49.6 44.5
August	0.787 0.794 0.846	73.8 79.1 75.6	1.1 0.5 4.2	39.5 41.3 35.9
September	0.732 0.702 0.727	74.8 65.7 77.4	2.7 -1.4 -1.7	46.5 38.7 44.4
October	0.706 0.687 0.666	89.1 85.5 100.6	10.1 20.0 27.6	55.5 52.5 60.5
November	0.661 0.689 0.724	110.2 95.0 102.7	21.5 20.8 25.5	71.3 60.4 64.7
December	0.723 0.714 0.726	98.7 98.6 102.5	5.2 18.3 22.1	64.8 63.6 65.5
January	0.704 0.744 0.682	108.4 115.6 116.8	10.5 3.9 9.3	69.5 76.6 75.5
February	0.695 0.507 0.670	106.1 120.4 113.3	6.6 3.7 13.2	68.2 82.3 78.9
March	0.664 0.654 0.628	115.0 124.5 128.4	10.0 18.6 4.0	77.2 83.6 85.1
April	0.675 0.746 0.735	110.8 107.8 110.0	1.1 10.0 2.9	74.1 68.8 68.6
May	0.779 0.785 0.834	102.9 89.8 99.6	-0.6 1.2 6.0	62.8 54.5 55.2

during the austral spring and in the northern Amazon during the austral summer as compared to the ENSO neutral year (Fig. 2), while the La Niña year (Fig. S3) exhibits weakest precipitation from October to January among the three years in the southeast region. The model reproduces the observed sub-seasonal and seasonal variabilities for these two years as well (Figs. S2–S3), like the ENSO neutral year. In general, the impact of ENSO phases is properly simulated. The statistics of monthly precipitation (Table 2) suggest little dependency of model performance on the ENSO phase.

The annual precipitation from the WRF simulation and IMERG observation for the three water years is displayed in Fig. 3, along with the Pearson correlation coefficient, areal mean difference, MAE, and RMSE in Table 3. Despite an overall similarity in spatial patterns, including the strong equatorial precipitation along the ITCZ and the precipitation band stretching from the central Amazon into the Atlantic Ocean along the SACZ, observations show apparent differences between the three water years (left column), indicative of the impact of ENSO phases. For instance, the Amazon Basin is comparatively wetter in the La Niña year than in the EI Niño year, and the opposite occurs for the La Plata Basin, with the ENSO neutral year being the average situation. These interannual contrasts are well captured by the model, and the tropical precipitation hot spots along the Colombian coast and over southwestern Colombia and nearby areas are reasonably replicated. Irrespective of the ENSO phase, however, WRF overestimates the annual orographic precipitation over both the tropical Andean Mountains and Guyana Highlands and parts of Brazil but underestimates the precipitation in part of tropical Atlantic coastal region and most of southern South America. The widespread wet biases in the central Amazon and localized dry biases near the equatorial Atlantic coast are seemingly more significant in the EI Niño year, in alignment with the slightly lower pattern correlation and higher absolute bias.

Figs. 4–5 present a comparison of annual total precipitation between WRF and gauge observation at station sites. The simulated spatial distribution shows a good agreement with observations (Fig. 4a-b). Especially, the model captures the heavy precipitation observed in the western Amazon Basin and southern Andes, as well as relatively light precipitation in southeastern Brazil. Disparities include the large positive biases in the tropical Andes and eastern Brazil (> 400 mm) and the negative bias in southern Brazil (Fig. 4c), consistent with the comparison against the IMERG data (Fig. 3c). The scatter plot (Fig. 5a) reveals a good one-to-one correspondence between the simulated and observed annual precipitation with a Pearson correlation of 0.8 and mean difference of 164 mm. Additionally, the simulation is skillful at reproducing the monthly precipitation totals averaged at all sites and the annual cycle (Fig. 5b), regardless of the wet bias for all months, particularly during the November–March rainy season.

The simulated and observed frequency of wet days and precipitation intensity for the ENSO neutral year are illustrated in Fig. 6. Herein, a wet day is defined as a day with daily precipitation accumulation greater than 1 mm and its frequency is calculated as the percentage of wet days with respect to the total number of days, whereas the corresponding mean intensity represents the daily precipitation amount averaged over all wet days. It is readily seen that the annual mean precipitation distributions (Fig. 3c) are mostly determined by precipitation occurrences, weakly correlated with the intensity. Overall, the spatial pattern of precipitation frequency is remarkably similar between the model and IMERG, with maxima in northwestern Amazon and Colombian Pacific coast and minima in northern Chile (Fig. 6a-b). The observed and simulated precipitation intensity are similarly characterized by weaker spatial variabilities in the tropics and subtropics, with a maximum value in the mid-latitude region, the La Plata Basin (Fig. 6d-e). Despite the good spatial agreement with observations, the simulation seems to produce too-few precipitation days (Fig. 6c) with too-strong intensity (Fig. 6f) across most of the continent. There is an underestimation of

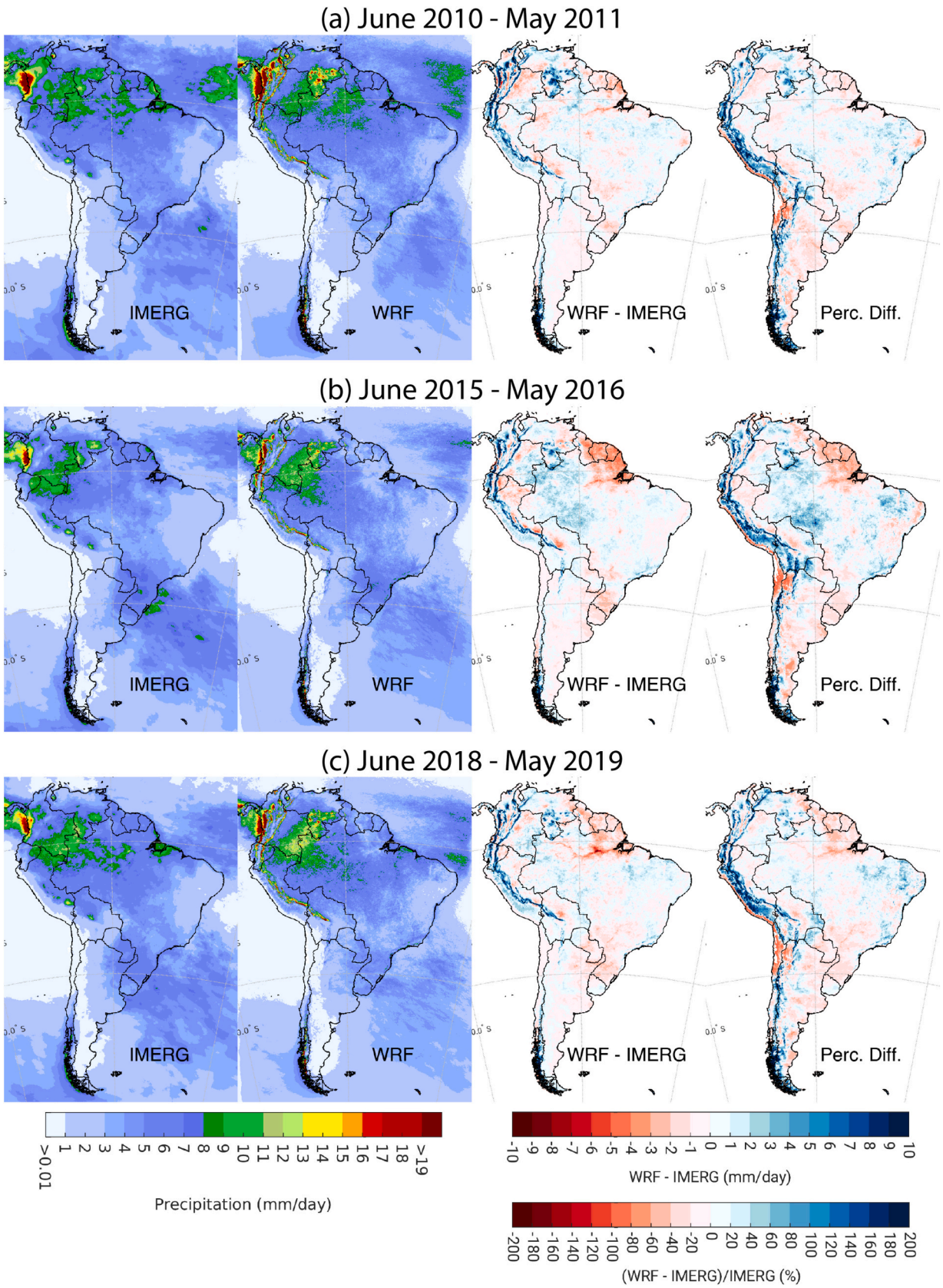

Fig. 3. Comparison of annual mean daily precipitation (mm day^{-1}) between IMERG (1st column) and simulation (EXP1–3; 2nd column) for (a) June 2010 – May 2011, (b) June 2015 – May 2016, and (c) June 2018 – May 2019. The 3rd and 4th columns show absolute and percent difference between model and IMERG over land. The pattern correlation coefficient, mean bias, MAE, and RMSE averaged over land points are presented in Table 3 for each water year.

Table 3
Statistical results of annual mean daily precipitation (mm day^{-1}) over land points of the model domain, including Pearson correlation coefficient, root mean square error (RMSE), mean bias, and mean absolute error (MAE) with respect to IMERG for various experiments (see Table 1).

Experiment	Corr. Coef.	RMSE (mm day^{-1})	Mean bias (mm day^{-1})	MAE (mm day^{-1})
EXP1	0.780	1.98	0.21	1.09
EXP2	0.744	1.97	0.24	1.16
EXP3	0.797	2.11	0.34	1.07
EXP4	0.769	2.08	0.22	1.05
EXP5	0.736	2.22	0.37	1.26
EXP6	0.737	1.87	−0.35	1.17
EXP7	0.710	2.04	−0.92	1.45
EXP8	0.799	1.92	0.03	1.04

intensity over the La Plata basin, with some overestimation of frequency in northern Argentina. An overestimate of both frequency and intensity dominates the Andes, accounting for the large wet bias therein (Fig. 3c), while the wet bias in Amazon, where the frequency is underpredicted, can be solely attributed to the overpredicted intensity. The same conclusions are effective for the two years of different ENSO phases (Figs. S4–S5).

The probability distribution of daily precipitation in Fig. 7a provides an evaluation of the model skill at generating the full spectrum of precipitation intensity over the continent, showing reasonable consistency between the simulation and observation. Though the simulation tends to underestimate weak precipitation days (< 20 mm day^{-1}) and overly produce heavy precipitation days (> 20 mm day^{-1}). Larger differences between model and IMERG are witnessed for the probability distribution of hourly precipitation (Fig. 7g), characteristic of an underprediction of wet hours below 7 mm h^{-1} and an overprediction of wet hours above 7 mm h^{-1}. Of note is that the less favorable agreement in hourly precipitation could partly stem from the relatively high uncertainty of the satellite precipitation at shorter time scales.

As anticipated, both the probability distribution and the model performance vary across various climate zones (Fig. 7b-f, h-l). As evidenced in Fig. 7b and h for Northern South America (NSA) and in Fig. 7c and i for Northwest South America (NWS), the low-latitude regions feature an overestimate of intense precipitation frequency and an underestimate of weak precipitation frequency for both daily and hourly precipitation, a pattern that largely aligns with the mean continental-scale characteristics discussed earlier (Fig. 7a, g). The other two tropical and subtropical regions, South American Monsoon (SAM) and Northeast South America (NES), are not shown, as they closely resemble NSA. A notably better agreement between the simulation and observations is observed in the mid-latitude region, Southeast South America (SES) (Fig. 7d, j). Additionally, the model performs reasonably well in the southern mountainous region, Southwest South America (SWS) (Fig. 7e, k). Unlike all other regions, the simulation tends to overestimate precipitation occurrence across nearly the entire intensity spectrum in the high-latitude region, Southern South America (SSA) (Fig. 7f, l), where snowfall predominates.

3.2. Diurnal cycle of summer precipitation

The diurnal cycle is a well-known solar heating forced mode of variability in the surface and atmospheric fields (Yang and Slingo, 2001; Dai and Trenberth, 2004). Its accurate depiction in numerical models requires the realistic representation of various components and their interactions of the Earth climate system, and thus is an important aspect of evaluation of the model physics. Fig. 8 compares the diurnal attributes of precipitation over the austral summer season (December – February) for the ENSO neutral year, including the timing of maximum hourly accumulated precipitation and the amplitude. [On average, local solar time (LST) is approximately 4 h behind UTC, namely, LST = UTC – 4.] In observations (Fig. 8b) the continent exhibits a rich diversity of regional diurnal variations due to the modulations associated with topography, land-sea contrast, land surface heterogeneity, convective storm propagation and many other processes. For the most part, the afternoon-evening peak dominates the inland region, the high mountains, and the Atlantic coast, resulting from the thermodynamical response in the planetary boundary layer to daytime solar heating cycle. Exceptions include 1) the nocturnal peak in the foothills of the Andes and part of northwestern Brazil; 2) the coherent eastward delayed timing over Argentina, which is a manifestation of propagating convection starting at the leeside in the evening and reaching the coast in the following morning; and 3) the inland delayed occurrence of maximum precipitation near the tropical Atlantic coast, which is likely a signature of southwestward traveling convection initiated by the sea breeze circulation along the coast in the morning. The model is capable of simulating the complex diurnal pattern (Fig. 8a), such as the prevalent afternoon-evening occurrence of maximum precipitation across the continent and regional nighttime peak along the local valley, the foothill, and the inland area adjacent to the Atlantic coast. In particular, the reasonable replication of the coherent phase lag east of the southern Andes is indicative of the model's capability in simulating propagating mesoscale convective systems (Prein, 2024). The primary deficiency is the overprediction of afternoon occurrence of maximum precipitation over the western and central Amazon. Phase discrepancies are also discernible in subtropical Andes and Brazilian Highlands.

The amplitude of hourly precipitation is computed to measure the strength of diurnal signals, another attribute of diurnal cycle as well as the peak timing. Herein, the diurnal amplitude is defined as the difference between daily maximum (P_{max}) and minimum (P_{min}) hourly precipitation normalized by the daily mean precipitation amount (P_{mean}), i.e., $(P_{max}\text{-}P_{min})/(2P_{mean})$x100%. As shown in Fig. 8d, the strongest diurnal signals are observed in northern Colombia and Venezuela, Chile, and central Argentina, with the weakest signals in the Amazon. These regional contrasts are well captured in the simulation (Fig. 8c), even though the model overly estimates the diurnal amplitude over most of the continent. In closing, the 4-km WRF model with explicit convection performs reasonably well at representing the observed diurnal variation of precipitation, which is further confirmed by the equally impressive performance in the other two summers (Figs. S6–S7).

3.3. Deep convective clouds (DCC)

South America is a hotspot for the occurrence of MCSs, where they contribute more than 50 % to annual total precipitation over most of Amazon and Colombian Pacific and up to 80 % in Argentina (Nesbitt et al., 2006; Feng et al., 2021; Prein et al., 2023; Jaramillo et al., 2017). As such, deep convective clouds (DCCs) in South America provide a key test bed for evaluating the convection-permitting climate simulations such as the present continental-scale simulations. In this study, we were not able to track MCS adequately due to the three hourly outputs of the 12 km simulation. Therefore, we decided to identify DCC characteristics at every model output time step without connecting clouds in time. We used the Multi-Object Analysis of Atmospheric Phenomenon (MOAAP; Prein et al., 2023) algorithm to identify DCCs with cloud top temperatures that are colder than 241 K and feature an overshoot being colder than 221 K. MOAAP uses a watershed method to separate large cloud shields into smaller clusters as seen in the example in Fig. S8. We use the IMERG precipitation data (Huffman et al., 2019) and the NASA Global Merged IR V1 infrared brightness temperature data (Janowiak et al., 2017) as observational reference and conservatively remap all datasets to the common grid of the 12 km WRF simulation before the analysis. We perform the analysis on the 6th IPCC Assessment Report regions that intersect with our modeling domain (see Fig. S1).

The size distribution of DCCs is similar between the observation, 4 km simulation (EXP1), and 12 km simulation (EXP6) for clouds smaller than 200,000 km^2 in the Northern South America (NSA) region (Fig. 9a).

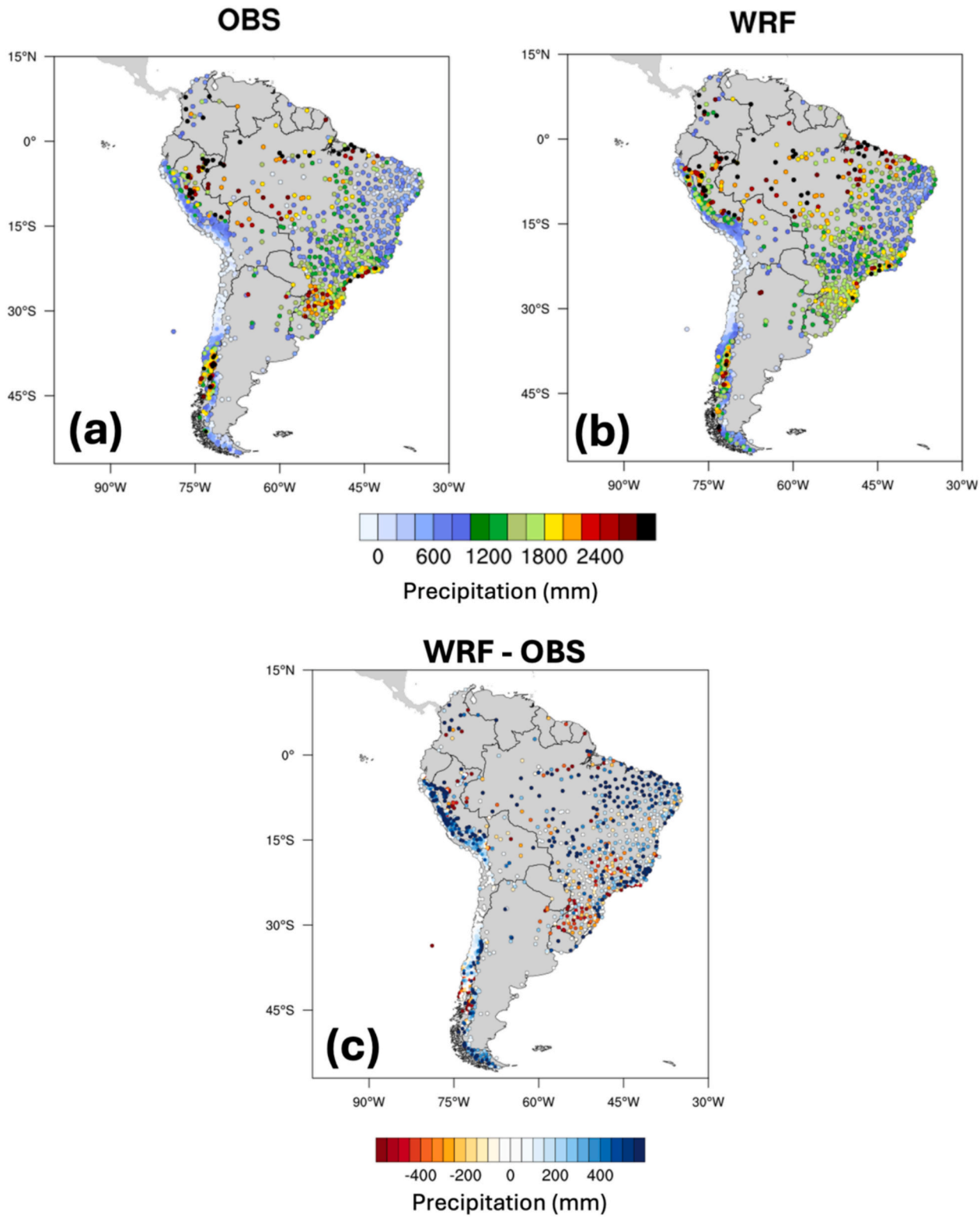

Fig. 4. Annual total precipitation (mm) of the 2018–2019 water year at the gauge sites for (a) observation and (b) simulation (EXP1). (c) Precipitation difference (mm) between simulation (EXP1) and observation.

Frequency of larger clouds is overestimated in the 4 km simulation while the 12 km simulation continues to agree well with observations. In the Southeast South America (SES) region (Fig. 9b) both simulations slightly underestimate the frequency of DCCs except for small clouds. Larger clouds are more realistically simulated in the 4 km simulation.

The largest fraction of precipitation is contributed by DCCs of about 50,000 km^2 size in NSA (Fig. 9c) and 50,000—150,000 km^2 in SES (Fig. 9d) according to observation. The 4 km simulation captures the observed distribution in the NSA region well except for a higher contribution of small DCCs. The 12 km simulation underestimates the contribution frequencies across the entire spectra of cloud sizes. In the SES region, both simulations are underestimating the amount of

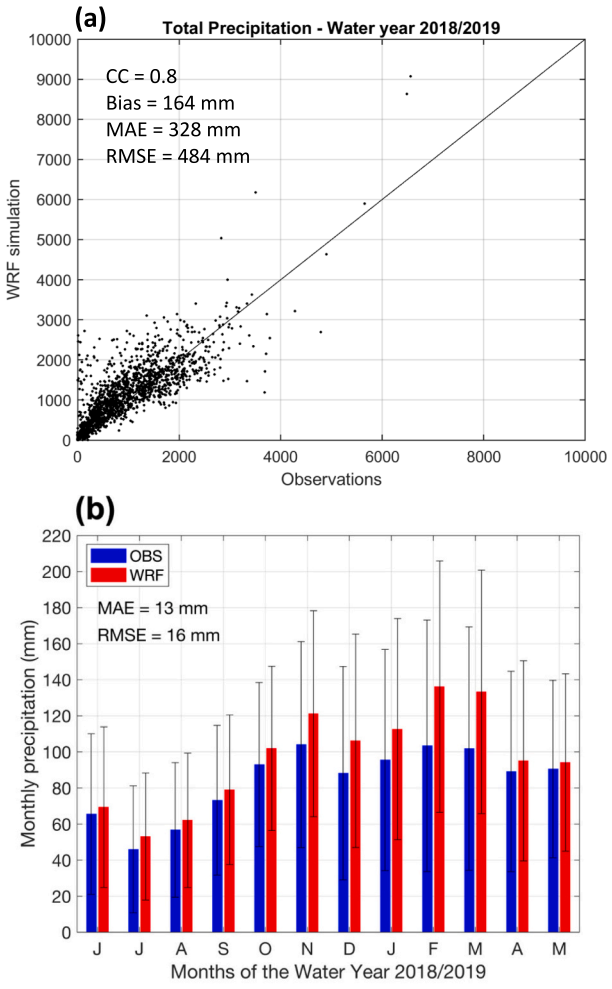

Fig. 5. (a) Scatterplot of simulated versus observed annual total precipitation (mm) at the gauge sites. (b) Histogram of monthly total precipitation (mm) for simulation (EXP1) and observation. Error bars in (b) show the standard deviation. The pattern correlation (CC), mean bias (Bias), mean absolute error (MAE), and RMSE are displayed at the upper left corner.

precipitation from DCC across all cloud sizes, although the 12 km run is closer to the observations for smaller clouds (Fig. 9d). It is unclear if the higher fraction of precipitation from small DCCs (particularly in the NSA region) in the 4 km model is a model bias or a deficiency in the observational capabilities of IMERG (e.g., Pradhan et al., 2022).

DCC mean precipitation is similar between observations and both simulations for large cloud systems in the NSA and SES region (Fig. 9e, f) while the 4 km simulation features much larger mean precipitation for small clouds than the observation and the 12 km simulation. It is uncertain whether this is a model or observational deficiency due to the difficulty in observing small, high-intensity precipitation areas in IMERG (Pradhan et al., 2022; Dominguez et al., 2023). In the SES region, the 4 km model mean precipitation statistics agree better with observations for smaller clouds except for the smallest cloud features.

The peak timing of DCC occurrence depends on the cloud size in the NSA region with larger clouds occurring during late night and early morning in the observation and 4 km simulation while small DCCs are most frequent during noon (Fig. 9g). This is due to the upscale growth of smaller systems toward larger-scale convective systems through the day and the nocturnal peak in MCS frequency in this region. The 12 km simulation is not able to capture these characteristics and features peak noon DCC frequencies independent of the cloud area. No clear dependency of timing on DCC size is visible in the SES region and all three datasets show similar characteristics (Fig. 9h).

Fig. S9 shows the DCC characteristics for all other IPCC regions that intersect with our modeling domain. We found the largest differences between the 4 km and 12 km simulation in the North Atlantic Ocean (NAO) and Equatorial Atlantic Ocean (EAO) region where the 4 km simulation clearly outperforms the 12 km simulation (except for mean precipitation and timing), although differences between the observation and the 4 km simulation persist. Both simulations struggle and largely underpredict the DCC frequency and precipitation contribution in the South Atlantic Ocean region. This is in line with the underestimate of MCS frequencies in 4 km model over this region as shown in Prein, 2024.

3.4. Surface air temperature

In this section, the simulated 2-m temperature is evaluated against ERA5 reanalysis data. Like the above precipitation analysis, the simulated temperature field is conservatively regridded to the ERA5 grid. The impact of elevation difference between the model and ERA5 is approximated by using the standard temperature lapse rate of 6.5 °C km^{-1}.

Fig. 10 shows the spatial distribution of seasonal mean daily 2-m maximum and minimum temperature (hereafter, T_{max} and T_{min} for brevity) differences with respect to ERA5 for the 2018/19 water year to validate WRF's capability in simulating near-surface temperatures. In general, ERA5 and WRF are in a good agreement, with an areal mean bias below 1 °C and a pattern correlation above 0.98 for both T_{max} and T_{min} for most seasons. The temperature difference across the continent is typically confined within ±2 °C, exhibiting a moderate seasonal dependency, especially for T_{max}. In JJA (Fig. 10a), T_{max} is characterized by a widespread cold bias except for north of the equator and the high Andes where a warm bias prevails. As the season progresses, the area of cold bias rapidly shrinks, while the warm bias constantly expands southward, occupying the whole Amazon basin in the spring (Fig. 10b) and further penetrating into the La Plata basin in the summer (Fig. 10c). With the seasonal progression into the fall (Fig. 10d), the warm bias shrinks, and the cold bias expands, with a spatial distribution comparable to the spring season. A year-around cold bias persists in the high latitudes south of 40°S, possibly attributed to the deficient snow physics in the land surface model as reported in He et al. (2019). It is interesting that the warm bias (Fig. 10) and precipitation (Fig. 2) experience a similar seasonal southward expansion and northward retreat, but there is no clear correlation between the temperature and precipitation biases. Contrastingly, a cold T_{min} bias dominates the continent throughout the year, with the bias being somewhat higher in the winter and spring than in the summer and fall. The EI Niño and La Niña years show quite similar spatial patterns and seasonal changes in the near-surface temperature bias (Figs. S10–S11).

The simulation and ERA5 agree reasonably well on the probability distribution of daily mean and instantaneous hourly 2-m temperatures (Fig. 11a-b), both being left-skewed and peaking around similar temperature values. Regardless, the simulation gives rise to a less elevated peak and wider tails, corresponding to an overprediction of both extreme cold and warm temperatures. Like the daily mean temperature, the daily maximum (Fig. 11c) and minimum temperature (Fig. 11d) are all left-tailed, with comparable peaks in the simulation and ERA5. But the overall agreement between the simulation and ERA5 is less favorable as compared to the daily mean, with T_{max} peaking at higher temperature and T_{min} peaking at lower temperature in the simulation than in ERA5, consistent with the prevailing T_{max} warm bias and T_{min} cold bias (Fig. 10). Another discrepancy is the broader tail in simulated T_{max} and T_{min}.

4. Sensitivity experiments

In addition to the three year-long simulations for different ENSO phases using 4-km WRF model, four sensitivity simulations, EXP4–7 (see Table 1), were conducted for the 2018/19 ENSO neutral year to examine the potential benefits of spectral nudging and convective

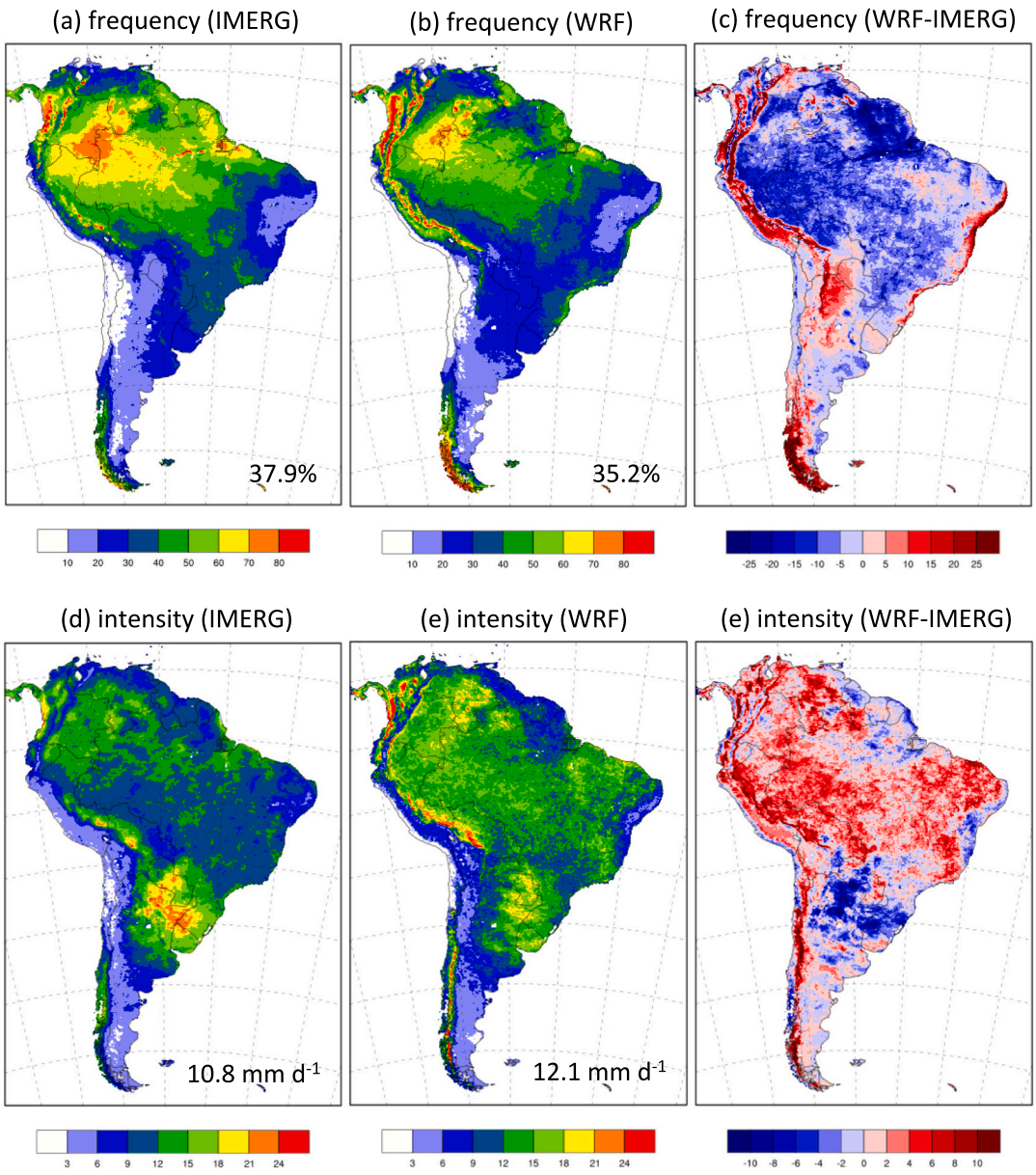

Fig. 6. The occurrence frequency of wet days (%; top) and precipitation intensity (mm day^{-1}; bottom) for the IMERG observation (left), the simulation (EXP1; middle), and the difference (model-IMERG; right) in the 2018/19 water year. The number is the land-point average value.

parameterization as well as the added value of the 4-km grid spacing relative to typical grid spacings used in traditional dynamical downscaling.

4.1. *Spectral nudging*

Spectral nudging has been widely applied to large-domain reanalysis-driven regional climate downscaling to enhance the consistency between simulated and observed large-scale fields, as well as to better capture the spatial and temporal characteristics of historical weather events and climate in the simulations. It can effectively eliminate climate drifting, mitigate various model biases, and reproduce synoptic weather systems (e.g., Miguez-Macho et al., 2004; Otte et al., 2012; Separovic et al., 2012; Pohl and Crétat, 2014; Omrani et al., 2015; Tang et al., 2016; Liu et al., 2017; Rasmussen et al., 2023). To examine how much benefit could be achieved from spectral nudging for the continental-scale simulation over South America, an experiment (EXP4 in Table 1) was performed with the same model configuration as in EXP1 but with the inclusion of spectral nudging. The specific setup was built upon the one used in the North American continental-scale downscaling (Liu et al., 2017; Rasmussen et al., 2023) and a series of test runs over the rainy period of November–December 2018, involving 1) nudging wind, geopotential and temperature variables at model level 12 (~1 km from the surface) and above; 2) a cutoff wavelength of ~1000 km; and 3) a nudging coefficient of 0.00005 for all variables.

Generally, the difference between the non-nudged and nudged simulations is insignificant, albeit non-negligible, in both the magnitude and spatial distribution of annual precipitation. As indicated in Fig. 12a-b, spectral nudging slightly reduces the high precipitation bias over the northwestern edge of the Amazon basin and south of the Amazon River and also the low precipitation bias along the Amazon valley and its northern flank, but it surprisingly worsens the wet bias over the ridges and slopes of the tropical and subtropical Andes. The domain mean precipitation and pattern correlation are little affected by the usage of spectral nudging (Table 3). This is also true for other precipitation attributes, such as frequency, intensity, and diurnal cycle and near-surface

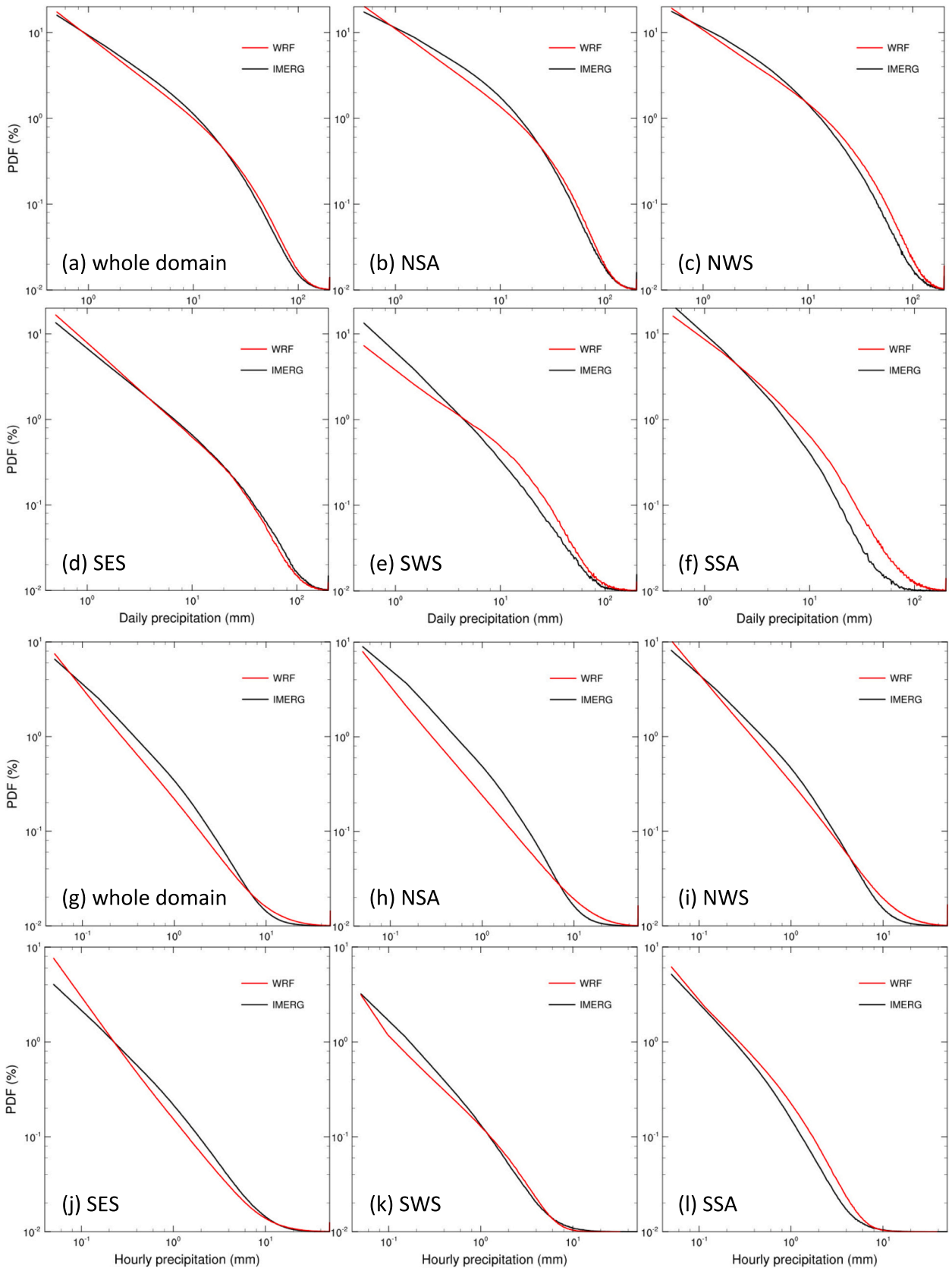

Fig. 7. The probability density function (PDF) of (a-f) daily and (g-l) hourly precipitation intensity (mm) over land points of model domain and different climate regions (see Fig. S1) for the 2018/19 water year. The red and black curves correspond to simulation (EXP1) and IMERG, respectively. (a,g) whole domain, (b,h) Northern South America (NSA), (c,i) Northwest South America (NWS), (d,j) Southeast South America (SES), (e,k) Southwest South America (SWS), and (f,l) Southern South America (SSA). (For interpretation of the references to colour in this figure legend, the reader is referred to the web version of this article.)

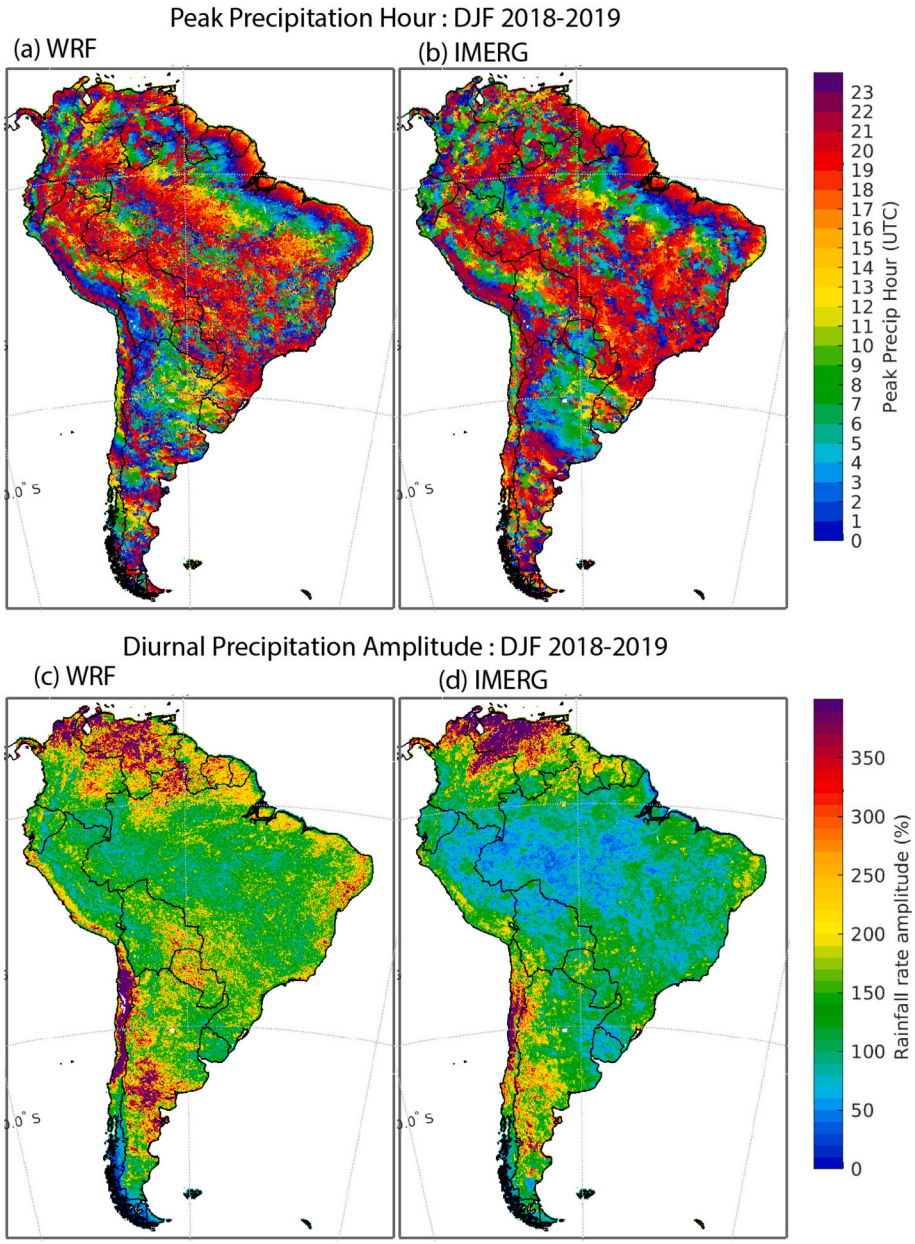

Fig. 8. Diurnal variation of precipitation over the austral summer (December–January-February) of the June 2018 – May 2019 water year. Top panels show the UTC hour of maximum precipitation for (a) simulation (EXP1) and (b) IMERG. Bottom panels show the diurnal amplitude of hourly precipitation for (c) simulation (EXP1) and (d) IMERG.

temperature (not shown).

The limited value of spectral nudging for the current continental-scale downscaling is in stark contrast to the significant benefit documented in previous studies over other parts of the world. For instance, applying spectral nudging to convection-permitting North America climate downscaling notably mitigates the warm-season temperature bias and improves the model skill in simulating climatological precipitation pattern (Liu et al., 2017). It was also reported that spectral nudging plays a critical role in reproducing the observed tropical multi-scale convective activities by the kilometer-scale WRF model (Liu and Moncrieff, 2015; Moncrieff et al., 2017; Chen et al., 2021). The smaller impacts of spectral nudging in the current simulation could be attributable to multiple factors. First, the skillful non-nudged simulation makes it difficult to further improve the model performance. Second, the uncertainties in the verification data complicate the assessment of nudging impact. For example, the deficient satellite precipitation product makes us less confident about the effect of the nudging induced precipitation enhancement over the Andes is suggestive of a degradation or an improvement. Third, the nudging performance relies on forcing data quality. Considering few sounding observations available for data assimilation, the reanalysis data over the South American continent may be not as reliable as over North America. Lastly, the trivial value from nudging in present experimentation could be associated with the presence of complex towering mountains. Recall that in spectral nudging, variables are transformed in the model coordinate by a fast-Fourier transform and then nudging is applied on selected large spatial scales only. In the presence of high mountains, however, the model coordinate is very different from the physical (i.e., height or pressure) coordinate, and accordingly the spectral decomposition and thus nudging would be physically less meaningful, and this caveat could hinder the nudging performance. In addition, it is possible that the current nudging configuration might not be the best-performing one to this geographical

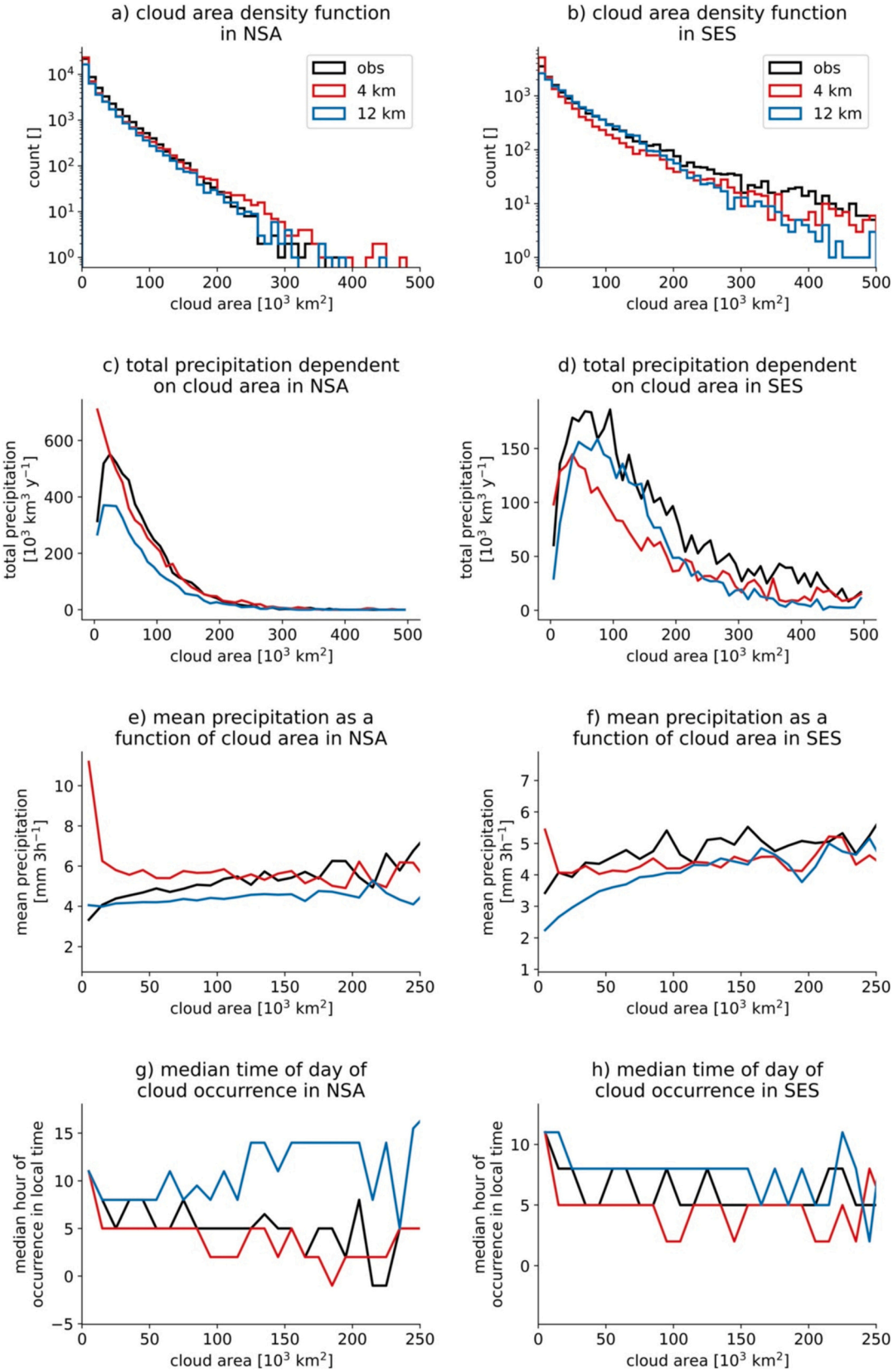

Fig. 9. Characteristics of deep convective clouds in observation (black), 12 km model simulation (EXP6, blue), and the 4 km simulation (EXP1, red) for the 2018/19 water year. The deep convective cloud area density function (a,b), the total (c,d) and mean (e,f) precipitation dependent on the cloud size, and the median diurnal hour of occurrence (g,h) dependent on size are shown for the Northern South America (NSA; left column) and Southeast South America (SES; right column) region. (For interpretation of the references to colour in this figure legend, the reader is referred to the web version of this article.)

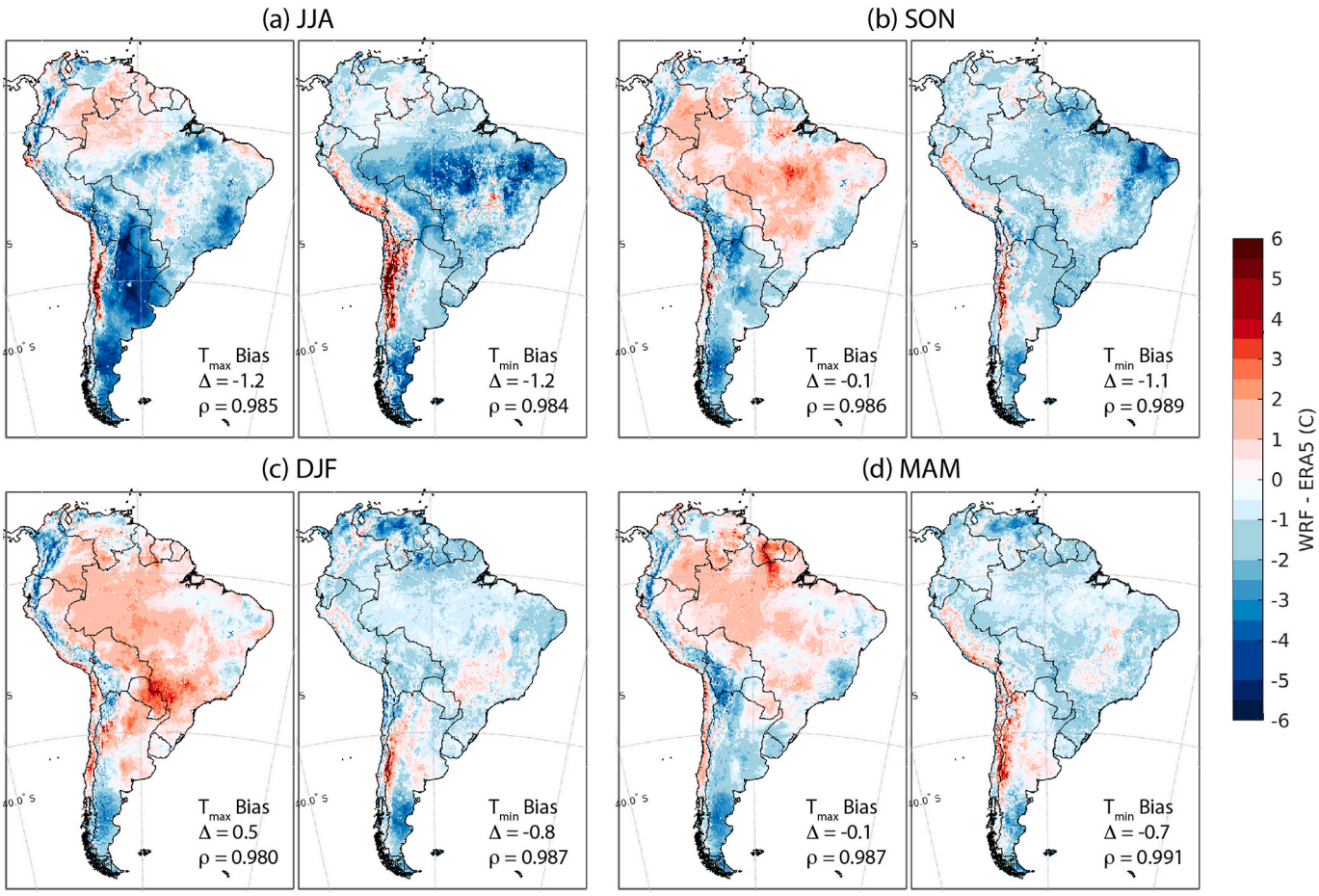

Fig. 10. Spatial distributions of seasonal mean daily 2-m maximum (left) and minimum (right) temperature differences between simulation (EXP1) and ERA5 (WRF-ERA5) for the 2018/19 water year. (a)-(d) correspond to the austral winter (JJA), spring (SON), summer (DJF), and autumn (MAM), respectively. Also shown are the Pearson correlation coefficient and mean difference (°C).

region, and therefore further testing may be needed.

4.2. Scale-dependent deep convection parameterization

The 4 km grid spacing used in the foregoing simulations falls into the convective grey zone resolution range (~1–10 km) where the grid length is close to the dimension of individual convective elements and convective processes are partially resolved, even though organized convective systems are represented explicitly. On the other hand, within the grey zone, small-scale convection would be poorly handled by traditional cumulus parameterization used in coarse resolution models since most of conventional closure assumptions break down. As such, numerous efforts have been made to enable traditional parameterizations to possess a scale-aware capability such that their validity is maintained across a range of grid spacing, along with a smooth transition from fully parameterized to explicit convection (Arakawa and Wu, 2013; Grell and Freitas, 2014; Zheng et al., 2016; Yun et al., 2017; Kwon and Hong, 2017; Wang, 2022). Previous testing in weather forecasting models demonstrated the values of such grid-scale-dependent parameterizations in improving various aspects of precipitation forecasts and modeling (e.g., Zheng et al., 2016; Kwon and Hong, 2017; Zhang et al., 2021). Notwithstanding, there is no consensus on whether subgrid convective processes should be parameterized in convection-permitting models, especially with grid-box lengths approaching the lower bound of the grey zone, as that used in the present study. Motivated by this curiosity, we carried out an experiment (EXP5 in Table 1) with a scale-aware convective parameterization. As detailed in Wang (2022), this scheme introduces a grid-size-dependent convective adjustment time scale into the Tiedtke convection parameterization (Tiedtke, 1989), which brings down the parameterized convective amount as grid length decreases.

Despite similar patterns and a mere ~3 % areal mean increase of precipitation amount as compared to the microphysics-only simulation (EXP1), the parameterization used in EXP5 causes a visible precipitation enhancement in most of the continent, especially over the Andes and southeastern Brazil, which further deteriorates the wet bias in these regions (Fig. 12c). An exception occurs along the equatorial Atlantic coast, where the rainfall is notably suppressed by the parameterization and thus the dry bias worsens. The overall small difference between the two simulations with different moisture physics treatment is not surprising in view of the parameterized convection accounting for 13.5 % of total amount only in the sensitivity simulation. In general, the inclusion of parameterization has little positive, or even negative value as demonstrated by somewhat higher mean bias and lower pattern correlation compared to EXP1 (Table 3). We also examined the precipitation frequency, intensity, and diurnal behavior in the sensitivity simulation (not shown) and found an overall resemblance to the microphysics-only simulation. Noticeable disparities are the domain wide increase in wet-day occurrence and decrease in precipitation intensity, attributable to the additional parameterized weak convective precipitation events.

As demonstrated in a recent grey-zone resolution modeling study of tropical convection (Liu et al., 2021), however, the model performance at 4-km grid spacing shows a weak but non-negligible dependence on the selection of convective parameterization. As such, the present comparison between simulations with and without parameterized convection would change if a different convection scheme were utilized as

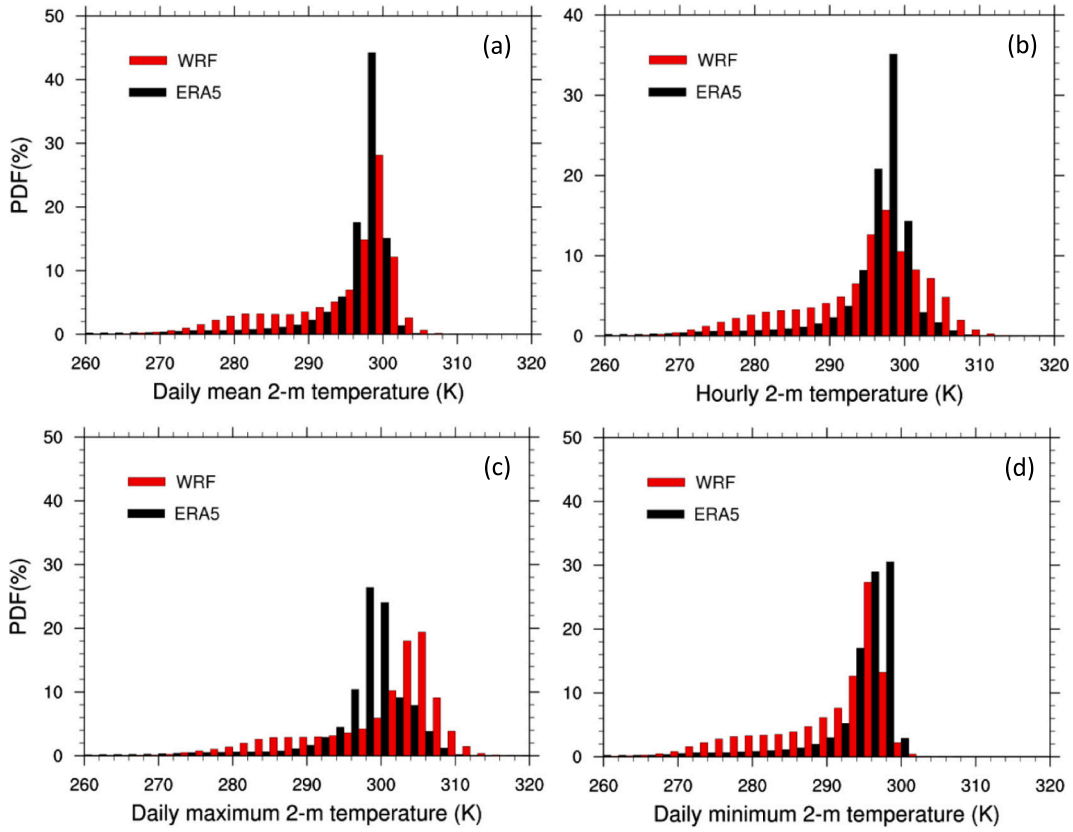

Fig. 11. Probability distribution of 2-m temperature (K) in simulation (EXP1) and ERA5 for the 2018/19 water year. (a) daily mean temperature (T_{mean}), (b) hourly temperature, (c) daily maximum temperature (T_{max}), and (d) daily minimum temperature (T_{min}).

evidenced in Liu et al. (2021).

4.3. Coarse resolution experiments

Previous studies in different geographical regions have shown consistent improvement in many aspects of model performance with the increasing resolution. Particularly, as compared against the coarse resolution models, convection-permitting models significantly improve the depiction of complex terrain and associated orographic precipitation, better the representation of diurnal cycle by bypassing conventional cumulus parameterization, and explicitly resolve organized convective systems and associated extreme weather among many others. To confirm if these advantages of convection-permitting model are valid to the South America region, we have conducted two coarser resolution experiments at a grid spacing of 12 and 24 km (EXP6–7 in Table 1), comparable to and even finer than the resolutions used in most of previous dynamical downscaling over South America (see the review by Ambrizzi et al., 2018). Distinct to the fully explicit convection in simulations at 4-km grid spacing, the subgrid deep convection is parameterized using the new Tiedtke scheme implemented in the WRF model by Zhang and Wang (2017).

The annual precipitation bias is contrasted between the three simulations with different grid spacing (i.e., EXP1, EXP6, and EXP7) in Fig. 12. Visually, the convection-permitting simulation is apparently closest to IMERG (Fig. 12a), outperforming the two coarser resolution simulations with parameterized convection (Fig. 12d-e), with the latter substantially underpredicting the tropical rainfall. Almost everywhere across the continent, larger grid spacing results in smaller precipitation amount. Consequently, the prevailing positive bias over many areas in the 4-km simulation is either much reduced or gives way to a prevalence of negative bias in the 12-km and 24-km simulations, and this resolution dependency is confirmed by the opposite signs of domain mean bias (Table 3). The superiority of the 4-km grid spacing is further attested by the statistical results, that is, higher spatial correlation, and lower mean bias and absolute bias of annual precipitation amount (Table 3), as well as the more accurate representation of precipitation frequency, intensity and diurnal variation (see Figs. 6, 8, and S12–S13). The 12-km simulation significantly overestimates the wet-day frequency and underestimates the precipitation intensity (Fig. S12), as well as the excessive afternoon timing of peak precipitation amount and frequency (Fig. S13) compared to IMERG (Fig. 8b), all of which reveal a worse performance relative to the 4-km simulation.

It is important to note that it is not only the resolution but also the representation of convective processes that affects the modeling results; that is, microphysics only at 4 km vs. microphysics plus convective parameterization at 12 and 24-km. Moreover, modeling results are very sensitive to deep convective parameterization. Accordingly, it should not be surprising that the performance of the 12-km and 24-km simulations and their difference relative to the 4-km simulation would change when a different convection scheme is used. But which parameterization performs best is beyond the scope of the present study.

5. Discussion and conclusions

In this study, the WRF model was configured with a continental-scale domain encompassing the South American continent at 4-km horizontal grid spacing for regional climate downscaling experimentation. The purpose is to assess the capability of convection-permitting WRF model in simulating regional precipitation and near-surface temperature, focusing on a best-suited setup established from our North America experience and a series of seasonal testing. Considering the significant influence of ENSO on the interannual variability, we have experimented three individual years, corresponding to different phases of ENSO, for general and robust conclusions. The main findings are as follows:

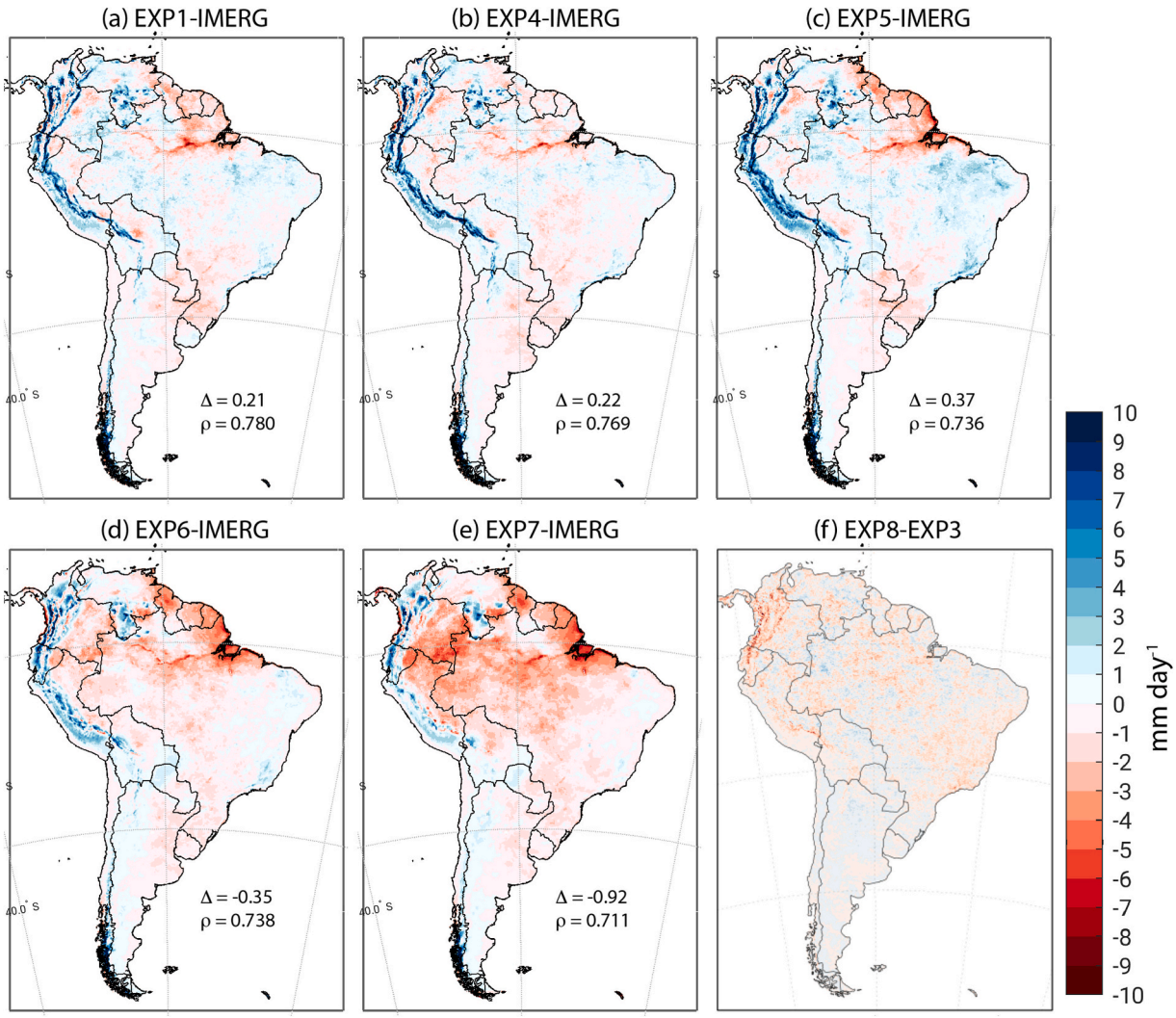

Fig. 12. (a)-(e) Annual mean precipitation difference from IMERG (mm day^{-1}) for the 2018/19 water year, corresponding to the simulation EXP1, the nudged simulation EXP4, the simulation EXP5 with convective parameterization applied, the simulation EXP6 at 12-km grid spacing, and the simulation EXP7 at 24-km grid spacing. Also shown are the Pearson correlation coefficient and areal mean bias relative to IMERG. (f) Annual mean precipitation difference (mm day^{-1}) for the 2010/11 water year between EXP8 and EXP3 (EXP8 - EXP3).

- The convection permitting WRF model realistically replicates the spatial distribution of annual, seasonal and sub-seasonal precipitation for all ENSO phases.
- The model closely captures the regional dry-wet transition, the seasonal migration of precipitation bands, and precipitation frequency and intensity, as well as the diverse diurnal patterns in association with the daily solar heating cycle, the sea-land contrast induced local circulation, the mountain-valley circulation, and propagating convection.
- The model displays good skill in representing the various attributes of observed deep convective clouds, except for the too-frequent occurrence of small clouds.
- WRF reasonably reproduces the seasonal near-surface temperature distribution, especially the large gradient across the narrow and steep mountains, as well as the probability distribution of daily mean and hourly temperatures.
- Overall, the model performance does not show apparent dependency on the ENSO phase.

In conclusion, regardless of the exclusion of spectral nudging, the overall promising performance is quite comparable to that over North America (e.g., Liu et al., 2017; Rasmussen et al., 2023), suggestive of the potential application of the tested model setup for long-term regional climate downscaling over the South American continent. Additional sensitivity experiments were conducted to quantify the potential value of spectral nudging and scale-sensitive convective parameterization, and the horizontal resolution impact. The results suggest the following:

- Limited benefit of spectral nudging, including the mitigation of the low rainfall bias in the vicinity of the equatorial Atlantic coast and the wet bias over most of the Amazon, is seen but is offset by the deteriorating orographic precipitation overprediction, leading to overall little improvement.
- Minimal benefit or even negative value is gained with the inclusion of a scale-aware convective parameterization, indicative of much needed improvement in the tested parameterization for grey-zone resolution.
- Coarser resolution simulations underperform the convection-permitting resolution simulation in terms of all evaluation metrics.

In summary, the sensitivity tests provide further support that the model configuration designed for the simulations of three individual years represents an optimal setup for regional climate downscaling applications over South America. This setup has been used for long-term

simulations over the continent, as described in Dominguez et al. (2023) and Liu et al. (2022).

Of notice is that the minimal benefit from spectral nudging in the present simulation contradicts the effectiveness of a similar spectral nudging configuration in alleviating some model deficiencies over North America (e.g., Liu et al., 2017). As discussed earlier, this geographic contrast may be partially attributed to the existence of high steep mountains, which physically invalidates the spectral decomposition on the model levels and thus the nudging efficacy, even though other aforementioned factors may play a role as well (see Section 4.1). In addition, the result from the convection-permitting resolution simulation with parameterized subgrid-scale convection should be viewed with caution, since the model performance is sensitive to the choice of convection scheme. Regardless, there is no consensus on the use of convective parameterization at the convection-permitting resolution (i.e., 1–4 km grid spacing), which has been excluded in most existing convection-permitting regional climate modeling, even though some weather forecasting type modeling studies indeed call for the inclusion of scale-aware convective parameterizations in grey-zone resolution simulations (e.g., Jeworrek et al., 2019; Zhang et al., 2021; Wang, 2022). The great sensitivity of model performance to grid spacing is perhaps less surprising. The remarkable superiority of 4-km grid spacing with respect to the 12-km and 24-km grid spacing is consistent with previous studies in other geographical regions (e.g., Ikeda et al., 2010; Kendon et al., 2012, 2014; Chan et al., 2014; Ban et al., 2014, 2021; Prein and Coauthors, 2015; Coppola and Coauthors, 2020). Arguably, kilometer-scale convection-permitting models are particularly advantageous over coarser resolution models over South America, considering the extremely complex terrain and the very dominant role of deep convection and abundant organized convective systems, all of which can be only adequately represented at sufficient fine resolution. Nevertheless, coarse resolution simulations with parameterized convection are greatly affected by the chosen convective parameterization scheme. It is likely that the performance would be improved if other parameterizations were used in our 12 and 24-km simulations.

Notwithstanding the promising performance, all simulations suffer

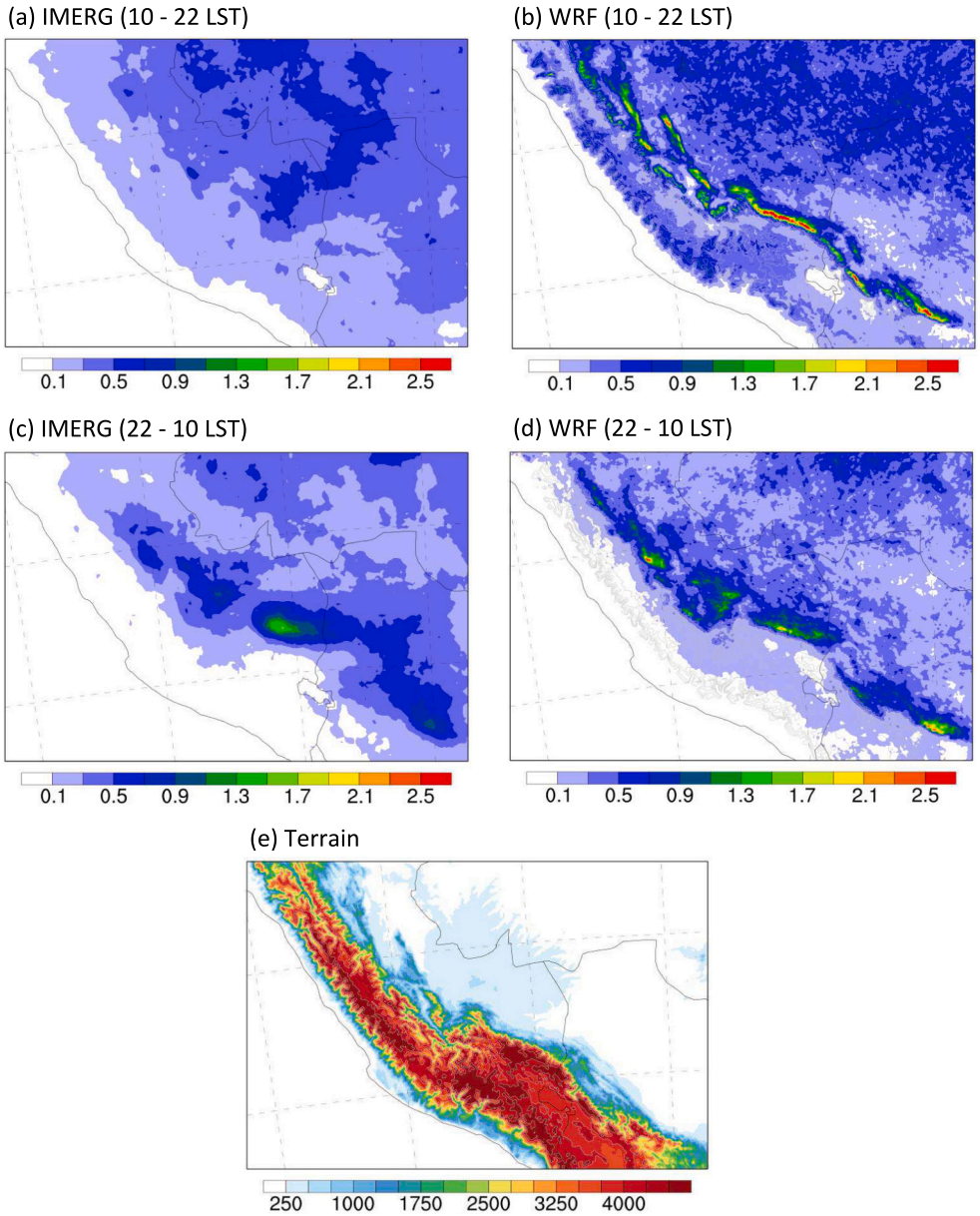

Fig. 13. Mean precipitation distribution (mm h^{-1}) in a region of subtropical Andes over daytime (10–22 LST) for (a) IMERG and (b) simulation (EXP1), and over nighttime (22–10 LST) for (c) IMERG and (d) simulation (EXP1). (e) Terrain (m) in the sub-domain.

some common deficiencies. The most striking one is the overprediction of precipitation over both the ridge and slopes of the Andes as compared to the IMERG observations. A wet bias, albeit comparatively much weaker, is also present over most of the Amazonian Basin. This year-round problem could result from the uncertainty in the verification data and/or the deficient model physics. Because of the shortage of reliable in situ observations over the high mountains, presently the model evaluation heavily relies on a newly created satellite precipitation product IMERG. A well-known advantage of this dataset is its complete global coverage with relatively high spatial and temporal resolutions. However, satellite estimates generally have large uncertainties in both the magnitude and variability (Sun et al., 2018; Vallejo-Bernal and co-authors, 2021) and difficulty representing precipitation in mountainous areas, where IR retrievals generally fail to capture light precipitation events and underestimate orographic rain, whereas passive microwave retrievals face challenges detecting orographic precipitation, especially in the cold season (Derin and Yilmaz, 2014). In short, because of large uncertainties in satellite-based precipitation products, the model discrepancies with respect to the IMERG data should be interpreted with caution.

In addition to the imperfect satellite retrieved precipitation, flawed treatment of subgrid physics in the WRF model may be blamed for the overprediction of orographic precipitation as well. Careful analysis over a subregion of subtropical Andes, where significant wet biases are observed, indicates that the spurious simulated precipitation mainly comes from excessive afternoon-evening convective precipitation (Fig. 13), likely a consequence of unrealistically strong surface solar radiative heating reported in a recent convection-permitting downscaling over North America using the same suit of physics parameterizations (Rasmussen et al., 2023). As well as insufficient cloudiness in the model, particularly in the mid-troposphere (Cintineo et al., 2014; Thompson et al., 2016; Kim et al., 2023), we speculate that the poor depiction of small-scale shallow boundary-layer convection and consequently its direct impact on insolation could play a role in the generation of excessive orographic precipitation. In the present model setup, the cloud fraction is determined by the grid-scale condensate generated from the microphysics scheme (Xu and Randall, 1996), implying that scattered shallow cumulus clouds in the daytime boundary layer would be likely underestimated because of the inability of the 4-km grid spacing to resolve these subgrid clouds. The under-representation of shallow convection, plus possible fewer clouds in the mid-troposphere, could lead to too much downward solar radiation reaching the ground and consequently development of overly strong thermal instability and orographic circulation during the daytime, in favor of convective genesis. As shown in Fig. 14, this hypothesis is supported by a comparison of surface downward solar radiation between the simulation and in situ observations at three sites in Chile, which reveals a clear overestimation of the observed shortwave flux by the WRF model. It should be mentioned that the excessive surface shortwave radiation and its potential linkage to the abundant afternoon precipitation were also suggested in other geographical regions (Yun et al., 2020, 2021; Liu et al., 2023). A thorough investigation into this model deficiency is important to model physics improvement but beyond the scope of the present study.

In addition to the aforementioned erroneous satellite estimates and the missing treatment of clouds, we speculate the lack of aerosol-cloud-radiation interactions may be partially responsible as well, as demonstrated in a surrogate CCN sensitivity experiment (EXP8 in Table 1), where the number of cloud droplets is modified from the default value of 100 per cc to 250 per cc to mimic an increase of CCN or aerosol concentration. It is shown that this microphysical change leads to an average ~ 7 % reduction of annual total precipitation relative to the baseline simulation EXP1, with the most significant decrease in the tropical and subtropical mountains (Fig. 12f). Improvements are measurable in all aspects of precipitation statistics (Table 3). A study over East Asia (Yun et al., 2020) also found that the inclusion of aerosol impact on cloud microphysics alleviated the excessive warm-season precipitation in WRF simulations. Taken together, the simulated high precipitation deficiency relative to satellite observations could arise from multiple factors, and its attribution study will be further pursued in our future endeavors.

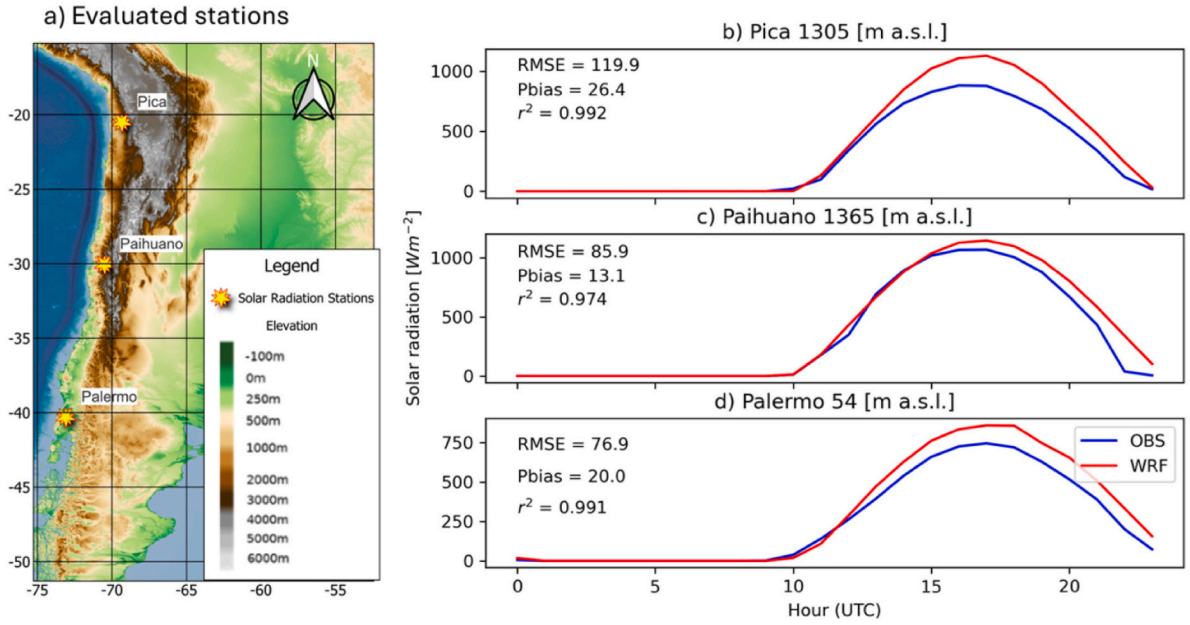

Fig. 14. Comparison of downward shortwave flux (DSWF, W m^{-2}) at the ground surface between WRF simulation (EXP1) and in situ observations at three stations. (a) Locations of the observational sites and terrain elevation; (b-d) Diurnal cycle of DSWF, averaged over December 2018 – February 2019, at each site. The root mean square error (RMSE), percent bias (Pbias), and coefficient of determination (r^2) at each site are shown in (b-d). The Pica and Palermo stations are operated by the Chilean Instituto de Investigaciones Agropecuarias (Agricultural Research Institute), while the Paihuano station is managed by the Chilean Water Agency (Dirección General de Aguas). The simulated DSWF is interpolated to each observation site using the nearest neighbor method.

CRediT authorship contribution statement

Changhai Liu: Conceptualization, Methodology, Formal analysis, Writing – original draft. **Kyoko Ikeda:** Formal analysis, Software, Data curation, Writing – review & editing. **Andreas Prein:** Conceptualization, Formal analysis, Writing – review & editing. **Lucia Scaff:** Investigation, Formal analysis, Writing – review & editing. **Francina Dominguez:** Conceptualization, Resources, Writing – review & editing. **Roy Rasmussen:** Project administration, Conceptualization, Writing – review & editing. **Yongjie Huang:** Software, Writing – review & editing. **Jimy Dudhia:** Software, Writing – review & editing. **Wei Wang:** Software, Writing – review & editing. **Fei Chen:** Writing – review & editing. **Lulin Xue:** Writing – review & editing. **Lluís Fita Borrell:** Investigation, Writing – review & editing. **Miguel Lagos-Zúñiga:** Investigation, Formal analysis, Writing – review & editing. **Waldo Lavado-Casimiro:** Investigation, Writing – review & editing. **Mariano Masiokas:** Investigation, Writing – review & editing. **Franciano Puhales:** Investigation, Writing – review & editing. **Leidy Johanna Yepes:** Investigation, Writing – review & editing.

Declaration of competing interest

The authors declare that they have no known competing financial interests or personal relationships that could have appeared to influence the work reported in this paper.

Data availability

The data presented in this study are available on request from the corresponding author. They are archived on NCAR Campaign storage and are distributable using Globus.

Acknowledgements

This research was supported by the National Science Foundation under the NCAR Water System Program. We would like to acknowledge high-performance computing support from Cheyenne (doi:https://doi.org/10.5065/D6RX99HX) provided by NCAR's Computational and Information Systems Laboratory's University Large Allocation, sponsored by the National Science Foundation (NSF) and award AGS 185270 from NSF. Miguel Lagos-Zúñiga acknowledges additional support from ANID-PIA Project AFB230001 (AMTC).

Appendix A. Supplementary data

Supplementary data to this article can be found online at https://doi.org/10.1016/j.atmosres.2025.107936.

References

Ambrizzi, T., Reboita, M.S., da Rocha, R.P., Llopart, M., 2018. The state-of-the-art and fundamental aspects of regional climate modeling in South America. Ann. N. Y. Acad. Sci. 1436 (1). https://doi.org/10.1111/nyas.13932.

Arakawa, A., Wu, C.-M., 2013. A unified representation of deep moist convection in numerical modeling of the atmosphere. Part I. J. Atmos. Sci. 70, 1977–1992. https://doi.org/10.1175/JAS-D-12-0330.1.

Arias, P.A., Garreaud, R., Poveda, G., Espinoza, J.C., Molina-Carpio, J., Masiokas, M., Van Oevelen, P.J., 2021. Hydroclimate of the Andes part II: hydroclimate variability and subcontinental patterns. Front. Earth Sci. 8, 505467.

Ban, N., Schmidli, J., Schär, C., 2014. Evaluation of the convection-resolving regional climate modeling approach in decade-long simulations. J. Geophys. Res. Atmos. 119 (13), 7889–7907. https://doi.org/10.1002/2014jd021478.

Ban, N., Caillaud, C., Coppola, E., et al., 2021. The first multi-model ensemble of regional climate simulations at kilometer-scale resolution, part I: evaluation of precipitation. Clim. Dyn. 57, 275–302. https://doi.org/10.1007/s00382-021-05708-w.

Barlage, M., Chen, F., Rasmussen, R., Zhang, Z., Miguez-Macho, G., 2021. The importance of scale-dependent groundwater processes in land-atmosphere interactions over the central United States. Geophys. Res. Lett. 48. https://doi.org/10.1029/2020GL092171 e2020GL092171.

Boulton, C., Good, P., Lenton, T., 2013. Early warning signals of simulated Amazon rainforest dieback. Theor. Ecol. 6, 373–384.

Cai, W., McPhaden, M.J., Grimm, A.M., et al., 2020. Climate impacts of the El Niño–Southern Oscillation on South America. Nat. Rev. Earth Environ. 1, 215–231. https://doi.org/10.1038/s43017-020-0040-3.

Chan, S.C., Kendon, E.J., Fowler, H.J., Blenkinsop, S., Roberts, N.M., Ferro, C.A.T., 2014. The value of high-resolution met office regional climate models in the simulation of multihourly precipitation extremes. J. Clim. 27 (16), 6155–6174. https://doi.org/10.1175/Jcli-D-13-00723.1.

Chen, C.-C., Richter, J.H., Liu, C., Moncrieff, M.W., Tang, Q., Lin, W., et al., 2021. Effects of organized convection parameterization on the MJO and precipitation in E3SMv1. Part I: mesoscale heating. J. Adv. Model. Earth Syst. 13, e2020MS002401. https://doi.org/10.1029/2020MS002401.

Cintineo, R., Otkin, J.A., Xue, M., Kong, F.Y., 2014. Evaluating the performance of planetary boundary layer and cloud microphysical parameterization schemes in convection-permitting ensemble forecasts using synthetic GOES-13 satellite observations. Mon. Weather Rev. 142 (1), 163–182. https://doi.org/10.1175/Mwr-D-13-00143.1.

Coppola, E., Coauthors, 2020. A first-of-its-kind multi-model convection permitting ensemble for investigating convective phenomena over Europe and the Mediterranean. Clim. Dyn. 55, 3–34. https://doi.org/10.1007/s00382-018-4521-8.

Dai, A., Trenberth, K.E., 2002. Estimates of freshwater discharge from continents: latitudinal and seasonal variations. J. Hydrometeorol. 3, 660–687. https://doi.org/10.1175/1525-7541(2002)003<0660:EOFDFC>2.0.CO;2.

Dai, A., Trenberth, K.E., 2004. The diurnal cycle and its depiction in the community climate system model. J. Clim. 17, 930–951. https://doi.org/10.1175/1520-0442(2004)017<0930:TDCAID>2.0.CO;2.

Derin, Y., Yilmaz, K.K., 2014. Evaluation of multiple satellite-based precipitation products over complex topography. J. Hydrometeorol. 15 (4), 1498–1516.

Dickinson, R.E., Errico, R.M., Giorgi, G.F., Bates, G.T., 1989. A regional climate model for the western United States. Clim. Chang. 15, 383–422.

Dominguez, F., Rasmussen, R., Liu, C.-H., Ikeda, K., Prein, A., co-authors, 2023. Advancing South American water climate science through multidecadal convection-permitting modeling. Bull. Am. Meteorol. Soc. 105, E32–E34. https://doi.org/10.1175/BAMS-D-22-0226.1.

Done, J., Davis, C.A., Weisman, M., 2004. The next generation of NWP: explicit forecasts of convection using the weather research and forecasting (WRF) model. Atmos. Sci. Lett. 5, 110–117.

Dussaillant, I., Berthier, E., Brun, F., Masiokas, M., Hugonnet, R., Favier, V., Ruiz, L., 2019. Two decades of glacier mass loss along the Andes. Nat. Geosci. 12 (10), 802–808. https://doi.org/10.1038/s41561-019-0432-5.

Espinoza, J.C., Garreaud, R., Poveda, G., Arias, P.A., Molina-Carpio, J., Masiokas, M., Scaff, L., 2020. Hydroclimate of the Andes part I: main climatic features. Front. Earth Sci. 8, 64. https://doi.org/10.3389/feart.2020.00064.

Feijoó, M., Solman, S., 2022. Convection-permitting modeling strategies for simulating extreme rainfall events over Southeastern South America. Clim. Dyn. 59 (9), 2549–2569. https://doi.org/10.1007/s00382-022-06226-z.

Feng, Z., Leung, L.R., Liu, N., Wang, J., Houze Jr., R.A., Li, J., Hardin, J.C., Chen, D., Guo, J., 2021. A global high-resolution mesoscale convective system database using satellite-derived cloud tops, surface precipitation, and tracking. J. Geophys. Res. Atmos. 126 (8), e2020JD034202.

Field, C.B., Behrenfeld, M.J., Randerson, J.T., Falkowski, P., 1998. Primary production of the biosphere: integrating terrestrial and oceanic components. Science 281 (5374), 237–240. https://doi.org/10.1126/science.281.5374.237.

Garreaud, R.D., Vuille, M., Compagnucci, R., Marengo, J., 2009. Present-day South American climate. Palaeogeogr. Palaeoclimatol. Palaeoecol. 281 (3–4), 180–195. https://doi.org/10.1016/j.palaeo.2007.10.032.

Gateño, F., Mendoza, P.A., Vásquez, N., Lagos-Zúñiga, M., Jiménez, H., Jerez, C., Montserrat, S., 2024. Screening CMIP6 models for Chile based on past performance and code genealogy. Clim. Chang. 177 (6), 87. https://doi.org/10.1007/s10584-024-03742-1.

Giorgi, F., 2019. Thirty years of regional climate modeling: where are we and where are we going next? J. Geophys. Res. Atmos. 124, 5696–5723. https://doi.org/10.1029/2018JD030094.

Giorgi, F., Bates, G.T., 1989. The climatological skill of a regional model over complex terrain. Mon. Weather Rev. 117, 2325–2347.

Grell, G.A., Freitas, S.R., 2014. A scale and aerosol aware stochastic convective parameterization for weather and air quality modeling. Atmos. Chem. Phys. 14, 5233–5250. https://doi.org/10.5194/acp-14-5233-2014.

Grimm, A.M., Zilli, M.T., 2009. Interannual variability and seasonal evolution of summer monsoon rainfall in South America. J. Clim. 22, 2257–2275. https://doi.org/10.1175/2008JCLI2345.1.

Guo, Z., Fang, J., Sun, X., Tang, J., Yang, Y., Tang, J., 2020. Decadal long convection-permitting regional climate simulations over eastern China: evaluation of diurnal cycle of precipitation. Clim. Dyn. 54 (9). https://doi.org/10.1007/s00382-019-05061-z.

Halladay, K., Kahana, R., Johnson, B., et al., 2023. Convection-permitting climate simulations for South America with the Met Office Unified Model. Clim. Dyn. 61, 5247–5269. https://doi.org/10.1007/s00382-023-06853-0.

He, C.-L., Chen, F., Barlage, M., Liu, C.-H., Newman, A., Tang, W., Ikeda, K., Rasmussen, R., 2019. Can convection-permitting modeling provide decent precipitation for offline high-resolution snowpack simulations over mountains? JGR-Atmos. https://doi.org/10.1029/2019JD030823.

Hersbach, H., Co-authors, 2010. The ERA5 global reanalysis. Q. J. R. Meteorol. Soc. 146, 1999–2049. https://doi.org/10.1002/qj.3803.

Hong, S.-Y., Noh, Y., Dudhia, J., 2006. A new vertical diffusion package with an explicit treatment of entrainment processes. Mon. Weather Rev. 134 (9), 2318–2341. https://doi.org/10.1175/MWR3199.1.

Huang, Y., Xue, M., Hu, X., Matin, E., Novoa, H., McPherson, R., Liu, C., Chen, M., Hong, Y., Perez, A.V., Morales, I., Ticona, J.L., Flores, A.J., 2024a. Increasing frequency and precipitation intensity of convective storms in the Peruvian Central Andes: Projections from convection-permitting regional climate simulations. Quarterly Journal of the Royal Meteorological Society 1–20. https://doi.org/10.1002/qj.4820.

Huang, Y., Xue, M., Hu, X., Matin, E., Novoa, H., McPherson, R., Liu, C., Ikeda, K., Rasmussen, R., Prein, A.F., Perez, A.V., Morales, I., Ticona, J.L., Flores, A.J., 2024b. Characteristics of Precipitation and Mesoscale Convective Systems over the Peruvian Central Andes in Multi 5-Year Convection-Permitting Simulations. Journal of Geophysical Research: Atmospheres 129. https://doi.org/10.1029/2023JD040394 e2023JD040394.

Huang, Y., Xue, M., Hu, X., Matin, E., Novoa, H., McPherson, R., Perez, A., Morales, I., 2023. Convection-Permitting Simulations of Precipitation over the Peruvian Central Andes: Strong Sensitivity to Planetary Boundary Layer Parameterization. Journal of Hydrometeorology 24, 1969–1990. https://doi.org/10.1175/JHM-D-22-0173.1.

Huffman, G.J., Bolvin, D.T., Braithwaite, D., Hsu, K., Joyce, R., Kidd, C., Nelkin, E.J., Sorooshian, S., Tan, J., Xie, P., 2019. Algorithm Theoretical Basis Document (ATBD) Version 5.2 for the NASA Global Precipitation Measurement (GPM) Integrated Multi-satellitE Retrievals for GPM (I-MERG). GPM. Project 38. https://pmm.nasa.gov/sites/default/files/document_files/IMERG_ATBD_V6.pdf.

Iacono, M.J., Delamere, J.S., Mlawer, E.J., Shephard, M.W., Clough, S.A., Collins, W.D., 2008. Radiative forcing by long-lived greenhouse gases: calculations with the AER radiative transfer models. J. Geophys. Res. 113, D13103. https://doi.org/10.1029/2008JD009944.

Ikeda, K., Rasmussen, R., Liu, C., et al., 2021. Snowfall and snowpack in the Western U.S. as captured by convection permitting climate simulations: current climate and pseudo global warming future climate. Clim. Dyn. 57, 2191–2215. https://doi.org/10.1007/s00382-021-05805-w.

Ikeda, K., Rasmussen, R., Liu, C., Gochis, D., Yates, D., Chen, F., et al., 2010. Simulation of seasonal snowfall over Colorado. Atmos. Res. 97 (4), 462–477. https://doi.org/10.1016/j.atmosres.2010.04.010.

Iturbide, M., Gutiérrez, J.M., Alves, L.M., Bedia, J., Cimadevilla, E., Cofiño, A.S., Cerezo-Mota, R., Di Luca, A., Faria, S.H., Gorodetskaya, I., Hauser, M., 2020. An update of IPCC climate reference regions for subcontinental analysis of climate model data: definition and aggregated datasets. Earth Syst. Sci. Data Discuss. 2020, 1–16.

Janowiak, J., Joyce, B., Xie, P., 2017. NCEP/CPC L3 Half Hourly 4km Global (60S-60N) Merged IR V1. Goddard Earth Sciences Data and Information Services Center, Greenbelt, MD, p. 4.

Jaramillo, L., Poveda, G., Mejía, J.F., 2017. Mesoscale convective systems and other precipitation features over the tropical Americas and surrounding seas as seen by TRMM. Int. J. Climatol. 37, 380–397.

Jeworrek, J., West, G., Stull, R., 2019. Evaluation of cumulus and microphysics parameterizations in WRF across the convective gray zone. Weather Forecast. 34, 1097–1115. https://doi.org/10.1175/WAF-D-18-0178.1.

Kain, J.S., Coauthors, 2008. Some practical considerations regarding horizontal resolution in the first generation of operational convection-allowing NWP. Weather Forecast. 23, 931–952. https://doi.org/10.1175/WAF2007106.1.

Kendon, E.J., Roberts, N.M., Senior, C.A., Roberts, M.J., 2012. Realism of rainfall in a very high-resolution regional climate model. J. Clim. 25, 5791–5806. https://doi.org/10.1175/JCLI-D-11-00562.1.

Kendon, E.J., Roberts, N.M., Fowler, H.J., Roberts, M.J., Chan, S.C., Senior, C.A., 2014. Heavier summer downpours with climate change revealed by weather forecast resolution model. Nat. Clim. Chang. 4, 570–576. https://doi.org/10.1038/nclimate2258.

Kim, J.-H., Dudhia, J., Ikeda, K., Rasmussen, R., Schneider, T., 2023. Evaluation of Clouds and Surface Solar Irradiance in the CONUS404 using the National Solar Radiation Database. AGU, San Francisco, 11-15 December 2023.

Kwon, Y.C., Hong, S.-Y., 2017. A mass-flux cumulus parameterization scheme across gray-zone resolutions. Mon. Weather Rev. 145, 583–598. https://doi.org/10.1175/MWR-D-16-0034.1.

Lenton, T.M., et al., 2008. Tipping elements in the Earth's climate system. Proc. Natl. Acad. Sci. USA 105, 1786.

Liu, C.-H., Moncrieff, M.W., 2015. Numerical Modeling of Multiscale Organized Convection and an Inertia-Gravity Wave Observed During YOTC. EGU, Vienna, 12-17 April 2015.

Liu, C.-H., Moncrieff, M.W., Tuttle, J.D., Carbone, R.E., 2006. Explicit and parameterized episodes of warm-season precipitation over the continental United States. Adv. Atmos. Sci. 23, 91–105.

Liu, C.H., Ikeda, K., Rasmussen, R., Barlage, M., Newman, A.J., Prein, A.F., et al., 2017. Continental-scale convection-permitting modeling of the current and future climate of North America. Clim. Dyn. 49 (1–2), 71–95. https://doi.org/10.1007/s00382-016-3327-9.

Liu, C.-H., Dudhia, J., Wang, W., Moncrieff, M.W., 2021. Tropical Convection Simulation in the Grey Zone: Impact of Horizontal Resolution and Convective Parameterization. AGU, New Orleans, 13–17 December 2021.

Liu, C., Ikeda, K., Rasmussen, R., et al., 2022. An Overview of Two-Decade-Long Convection Permitting Regional Climate Downscaling over the Continental South America. American Geophysical Union Fall Meeting. American Geophysical Union, Chicago, IL available at https://agu.confex.com/agu/fm22/meetingapp.cgi/Paper/1115319.

Liu, H., Liu, X., Liu, C., Yun, Y., 2023. High-resolution regional climate modeling of warm-season precipitation over the Tibetan Plateau: impact of grid spacing and convective parameterization. Atmos. Res. 281, 106498. https://doi.org/10.1016/j.atmosres.2022.106498.

Malhi, Y., et al., 2006. The regional variation of aboveground live biomass in old-growth Amazonian forests. Glob. Chang. Biol. 12, 1107–1138.

Masiokas, M.H., Rabatel, A., Rivera Ibáñez, Andrés, Ruiz, L., Pitte, P., Ceballos, J.L., Barcaza, G., Soruco, A., Bown, F., Berthier, E., Dussaillant, I., MacDonell, S., 2020. A review of the current state and recent changes of the Andean cryosphere. Front. Earth Sci. 8. https://doi.org/10.3389/feart.2020.00099.

Miguez-Macho, G., Stenchikov, G.L., Robock, A., 2004. Spectral nudging to eliminate the effects of domain position and geometry in regional climate model simulations. J. Geophys. Res. Atmos. 109 (D13). https://doi.org/10.1029/2003JD004495.

Miguez-Macho, G., Fan, Y., Weaver, C.P., Walko, R., Robock, A., 2007. Incorporating water table dynamics in climate modeling: 2. Formulation, validation, and soil moisture simulation. J. Geophys. Res. 112, D13108. https://doi.org/10.1029/2006JD008112.

Moncrieff, M.W., Liu, C., Bogenschutz, P., 2017. Simulation, modeling, and dynamically based parameterization of organized tropical convection for global climate models. J. Atmos. Sci. 74, 1363–1380. https://doi.org/10.1175/JAS-D-16-0166.1.

Nesbitt, S.W., Cifelli, R., Rutledge, S.A., 2006. Storm Morphology and Rainfall Characteristics of TRMM Precipitation Features. Monthly Weather Review 134 (10), 2702–2721. https://doi.org/10.1175/MWR3200.1.

Niu, G.Y., et al., 2011. The community Noah land surface model with multiparameterization options (Noah-MP): 1. Model description and evaluation with local-scale measurements. J. Geophys. Res. 116, D12109. https://doi.org/10.1029/2010JD015139.

Omrani, H., Drobinski, P., Dubos, T., 2015. Using nudging to improve global-regional dynamic consistency in limited-area climate modeling: what should we nudge? Clim. Dyn. 44 (5–6), 1–18. https://doi.org/10.1007/s00382-014-2453-5.

Otte, T.L., Nolte, C.G., Otte, M.J., Bowden, J.H., 2012. Does nudging squelch the extremes in regional climate modeling? J. Clim. 25 (20), 7046–7066. https://doi.org/10.1175/JCLI-D-12-00048.1.

Pohl, B., Crétat, J., 2014. On the use of nudging techniques for regional climate modeling: application for tropical convection. Clim. Dyn. 43 (5–6), 1693–1714. https://doi.org/10.1007/s00382-013-1994-3.

Portele, T.C., Laux, P., Lorenz, C., Janner, A., Horna, N., Fersch, B., Iza, M., Kunstmann, H., 2021. Ensemble-tailored pattern analysis of high-resolution dynamically downscaled precipitation fields: example for climate sensitive regions of South America. Front. Earth Sci. 9, 669427. https://doi.org/10.3389/feart.2021.669427.

Pradhan, R.K., Markonis, Y., Godoy, M.R.V., Villalba-Pradas, A., Andreadis, K.M., Nikolopoulos, E.I., Papalexiou, S.M., Rahim, A., Tapiador, F.J., Hanel, M., 2022. Review of GPM IMERG performance: a global perspective. Remote Sens. Environ. 268, 112754.

Prein, et al., 2024. Km-scale simulations of mesoscale convective systems over South America – a feature tracker intercomparison. J. Geophys. Res. 129. https://doi.org/10.1029/2023JD040254 e2023JD040254.

Prein, A.F., Coauthors, 2015. A review on regional convection-permitting climate modeling: demonstrations, prospects, and challenges. Rev. Geophys. 53, 323–361. https://doi.org/10.1002/2014RG000475.

Prein, A.F., Liu, C., Ikeda, K., Bullock, R., Rasmussen, R.M., Holland, G.J., et al., 2017. Simulating North American mesoscale convective systems with a convection-permitting climate model. Clim. Dyn. https://doi.org/10.1007/s00382-017-3993-2.

Prein, A.F., Mooney, P.A., Done, J.M., 2023. The multi-scale interactions of atmospheric phenomenon in mean and extreme precipitation. Earth's Future 11 (11), e2023EF003534.

Rasmussen, R., Liu, C.H., Ikeda, K., Gochis, D., Yates, D., Chen, F., et al., 2011. High-resolution coupled climate runoff simulations of seasonal snowfall over Colorado: a process study of current and warmer climate. J. Clim. 24 (12), 3015–3048. https://doi.org/10.1175/2010jcli3985.1.

Rasmussen, R.M., Chen, F., Liu, C.H., Ikeda, K., Prein, A., Kim, J., Schneider, T., Dai, A., Gochis, D., Dugger, A., Zhang, Y., Jaye, A., Dudhia, J., He, C., Harrold, M., Xue, L., Chen, S., Newman, A., Dougherty, E., Abolafia-Rosenzweig, R., Lybarger, N.D., Viger, R., Lesmes, D., Skalak, K., Brakebill, J., Cline, D., Dunne, K., Rasmussen, K., Miguez-Macho, G., 2023. CONUS404: The NCAR–USGS 4-km Long-Term Regional Hydroclimate Reanalysis over the CONUS. Bulletin of the American Meteorological Society 104 (8), E1382–E1408. https://doi.org/10.1175/BAMS-D-21-0326.1.

Rasmussen, R., Ikeda, K., Liu, C.H., Gochis, D., Clark, M., Dai, A.G., et al., 2014. Climate change impacts on the water balance of the Colorado headwaters: high-resolution regional climate model simulations. J. Hydrometeorol. 15 (3), 1091–1116. https://doi.org/10.1175/Jhm-D-13-0118.1.

Schär, C., Co-authors, 2020. Kilometer-scale climate models: prospects and challenges. Bull. Am. Meteorol. Soc. 101, 567–587. https://doi.org/10.1175/BAMS-D-18-0167.1.

Separovic, L., Elía, R.D., Laprise, R., 2012. Impact of spectral nudging and domain size in studies of RCM response to parameter modification. Clim. Dyn. 38 (7), 1325–1343. https://doi.org/10.1007/s00382-011-1072-7.

Skamarock, W., Klemp, J., Dudhia, J., Gill, D.O., Liu, Z., Berner, J., Wang, W., Powers, J. G., Duda, M.G., Barker, D., Huang, X.-Y., 2019. A Description of the Advanced Research WRF Model Version 4.1. NCAR Tech. Note NCAR/TN-556+STR,, 145. https://doi.org/10.5065/1dfh-6p97.

Solman, S.A., 2013. Regional climate modeling over South America: a review. Adv. Meteorol. 2013, 504357. https://doi.org/10.1155/2013/504357.

Stratton, R.A., Senior, C.A., Vosper, S.B., Folwell, S.S., Boutle, I.A., Earnshaw, P.D., et al., 2018. A Pan-African convection-permitting regional climate simulation with the met office unified model: CP4-Africa. J. Clim. 31 (9), 3485–3508. https://doi.org/10.1175/jcli-d-17-0503.1.

Sun, Q., Miao, C., Duan, Q., Ashouri, H., Sorooshian, S., Hsu, K.-L., 2018. A review of global precipitation data sets: data sources, estimation, and inter- comparisons. Rev. Geophys. 56, 79–107. https://doi.org/10.1002/2017RG000574.

Tang, J., Wang, S., Niu, X., Hui, P., Zong, P., Wang, X., 2016. Impact of spectral nudging on regional climate simulation over CORDEX East Asia using WRF. Clim. Dyn. 48 (7–8), 2339–2357. https://doi.org/10.1007/s00382-016-3208-2.

Tedeschi, R.G., Cavalcanti, I.F., Grimm, A.M., 2013. Influences of two types of ENSO on South American precipitation. Int. J. Climatol. 33 (6), 1382–1400. https://doi.org/10.1002/joc.3519.

Thompson, G., Field, P.R., Rasmussen, R.M., Hall, W.D., 2008. Explicit forecasts of winter precipitation using an improved bulk microphysics scheme. Part II: implementation of a new snow parameterization. Mon. Weather Rev. 136, 5095–5115. https://doi.org/10.1175/2008MWR2387.1.

Thompson, G., Tewari, M., Ikeda, K., Tessendorf, S., Weeks, C., Otkin, J., et al., 2016. Explicitly-coupled cloud physics and radiation parameterizations and subsequent evaluation in WRF high-resolution convective forecasts. Atmos. Res. 168, 92–104. https://doi.org/10.1016/j.atmosres.2015.09.005.

Tiedtke, M., 1989. A comprehensive mass flux scheme for cumulus parameterization in large-scale models. Mon. Weather Rev. 117, 1779–1800. https://doi.org/10.1175/1520-0493(1989)117<1779:ACMFSF>2.0.CO;2.

Vallejo-Bernal, co-authors, 2021. Ground validation of TRMM 3B43 V7 precipitation estimates over Colombia. Part I: monthly and seasonal timescales. Int. J. Climatol. 41 (1), 601–624.

Vera, C., Silvestri, G., Liebmann, B., González, P., 2006. Climate change scenarios for seasonal precipitation in South America from IPCC-AR4 models. Geophys. Res. Lett. 33. https://doi.org/10.1029/2006GL025759.

Wang, W., 2022. Forecasting convection with a "scale-aware" Tiedtke cumulus parameterization scheme at kilometer scales. Weather Forecast. 37, 1491–1507. https://doi.org/10.1175/WAF-D-21-0179.1.

Wang, Y.-G., Gerrts, B., Liu, C.-H., 2018. A 30-year convection-permitting regional climate simulation over the interior western United States. Part I: validation. Int. J. Climatol. 38 (1–2). https://doi.org/10.1002/joc.5527.

Xu, K.-M., Randall, D.A., 1996. A semiempirical cloudiness parameterization for use in climate models. J. Atmos. Sci. 53, 3084–3102. https://doi.org/10.1175/1520-0469(1996)053%3c3084:ascpfu%3e2.0.co;2.

Xue, Y., Janjic, Z., Dudhia, J., Vasic, R., de Sales, F., 2014. A review on regional dynamical downscaling in interseasonal to seasonal simulation/prediction and major factors that affect downscaling ability. Atmos. Res. 147-148, 68–85.

Yang, Z., Dominguez, F., 2019. Investigating land surface effect on the moisture transport over South America with a moisture tagging model. J. Clim. 32. https://doi.org/10.1175/JCLI-D-18-0700.1.

Yang, G.-Y., Slingo, J., 2001. The diurnal cycle in the Tropics. Mon. Weather Rev. 129, 784–801.

Yin, L., Fu, R., Shevliakova, E., Dickinson, R.E., 2013. How well can CMIP5 simulate precipitation and its controlling processes over tropical South America? Clim. Dyn. 41, 3127–3143. https://doi.org/10.1007/s00382-012-1582-y.

Yun, Y., Fan, J., Xiao, H., Zhang, G.J., Ghan, S.J., Xu, K.-M., et al., 2017. Assessing the resolution adaptability of the Zhang-McFarlane cumulus parameterization with spatial and temporal averaging. J. Adv. Model. Earth Syst. 9 (7), 2753–2770. https://doi.org/10.1002/2017ms001035.

Yun, Y., Liu, C., Luo, Y., Liang, X., Huang, L., Chen, F., Rasmussen, R., 2020. Convection-permitting regional climate simulation of warm-season precipitation over Eastern China. Clim. Dyn. https://doi.org/10.1007/s00382-019-05070-y.

Yun, Y., Liu, C., Luo, Y., Gao, W., 2021. Warm-season mesoscale convective systems over eastern China: convection-permitting climate model simulation and observation. Clim. Dyn. 57 (7), 1–19. https://doi.org/10.1007/s00382-021-05994-4.

Zhang, C., Wang, Y., 2017. Projected future changes of tropical cyclone activity over the western North and South Pacific in a 20-km-mesh regional climate model. J. Clim. 30, 5923–5941. https://doi.org/10.1175/JCLI-D-16-0597.1.

Zhang, X., Yang, Y., Chen, B., Huang, W., 2021. Operational precipitation forecast over China using the weather research and forecasting (WRF) model at a gray-zone resolution: impact of convection parameterization. Weather Forecast. 36, 915–928. https://doi.org/10.1175/WAF-D-20-0210.1.

Zheng, Y., Alpaty, K., Herwehe, J.A., Del Genio, A.D., Niyogi, D., 2016. Improving high-resolution weather forecasts using the weather research and forecasting (WRF) model with an updated Kain-Fritsch scheme. Mon. Weather Rev. 144 (3), 833–860. https://doi.org/10.1175/MWR-D-15-0005.1.